Title: Wildfire severity reshapes remotely sensed surface temperature and vegetation phenology in a Western Cascades forest ecosystem

Daniel M. Griffith[1]*
Christopher J. Still[2]
Matthew G. Betts[2]
Amelia Fitch[2]
Hannah R. Sachs[2]
Mark D Schulze[2]

[1] Department of Ecology and Evolution, Stony Brook University, Stony Brook, NY, USA. 11790
[2] Forest Ecosystems and Society, Oregon State University, Corvallis, OR, 97331

*Corresponding author
daniel.griffith@stonybrook.edu

This is a non-peer reviewed preprint submitted to EarthArXiv.

Words: ~9000
References: 51
Figures: 8
Tables: 1
Supplements: 1

Keywords: ECOSTRESS; HLS; land surface temperature; NIRv; phenology; wildfire; burn severity; LiDAR; H.J. Andrews Experimental Forest

Abstract

Wildfire reorganizes forests by altering canopy structure, surface energy balance, vegetation activity, and microclimate. However, these effects remain difficult to quantify across seasons, times of day, burn severities, and complex terrain. We used the 2023 Lookout Fire at the H.J. Andrews Experimental Forest, Oregon, to test how fire severity altered coupling between surface temperature and vegetation phenology. We integrated ECOSTRESS land surface temperature (LST), HLS-2 near-infrared reflectance of vegetation (NIRv), RAVG burn severity, Daymet climate, airborne LiDAR, and phenology observations. ECOSTRESS observations were standardized by harmonic regression for seasonal and diurnal acquisition timing. Post-fire warming was strongest in summer and increased with burn severity (1.5 °C increase for severe). High-severity areas warmed more than unburned areas, especially under high shortwave radiation, low rainfall, and high vapor pressure. Open vegetation cover was associated with warmer LST, whereas higher elevations were cooler. At phenology plots, ECOSTRESS LST generally exceeded instantaneous air temperature ($\Delta T = 0.55$), and burn severity steepened this relationship after fire (1 to 1.15 slope). HLS NIRv captured seasonal and disturbance-driven vegetation activity and was associated with Douglas-fir budbreak and summer temperature. Across the landscape, post-fire declines in NIRv were associated with warmer noon-standardized LST, and structural equation modeling indicated that reduced evapotranspiration largely mediated this relationship. Among the first to use ECOSTRESS observations, our study resolved seasonal and diurnal post-fire warming while linking thermal responses to satellite vegetation activity, LiDAR-derived structure, and field phenology. Together, these results show that wildfire severity reorganized thermal regimes across seasons and times of day, while vegetation phenology provided biological context for post-fire climate change.

1. Introduction

Rising temperatures, increasing summer drying, and changing disturbance regimes are reshaping forest ecosystems across western North America. In the Pacific Northwest, wildfire is increasingly important as a driver of forest structure, ecosystem function, and landscape heterogeneity (e.g., Halofsky *et al.*, 2018; Tepley *et al.*, 2018) (Halofsky *et al.*, 2020; Wasserman & Mueller, 2023; Busby *et al.*, 2023). Fire can alter canopy cover, vegetation composition, surface roughness, soil exposure, albedo, and hydrologic processes, with consequences for the surface energy balance and the thermal environments experienced by plants, soils, and regenerating communities (Chen *et al.*, 1992, 1999) (Sánchez *et al.*, 2015). These post-fire changes are unlikely to be spatially uniform (Gosnell *et al.*, 2020). Instead, they should depend on burn severity, pre-fire forest structure, topography, and seasonal climate, particularly during summer periods when radiation load and atmospheric water demand are high.

Land surface temperature (LST) provides an integrative measure of post-fire surface climate because it reflects the combined effects of radiation, vegetation structure, surface moisture, atmospheric conditions, and energy partitioning (Still *et al.*, 2019, 2021). Post-fire canopy loss can increase exposure of soil, woody debris, and understory vegetation to solar radiation, potentially producing warmer daytime surface temperatures than those observed under intact forest canopies. However, the magnitude of post-fire surface warming should vary across seasons and times of day. A fire effect that is weak or absent during cool, wet seasons may become pronounced during dry summer conditions, when reduced shading and altered surface properties amplify heating. Similarly, daytime warming may be far stronger than nighttime warming, making diurnal sampling central to the interpretation of post-fire thermal regimes.

Satellite thermal remote sensing provides an opportunity to quantify these patterns across landscapes, but the temporal structure of satellite observations strongly influences what can be inferred. Many long-running satellite thermal records are collected at fixed or near-fixed overpass times, which provide consistency but may miss the time of day when post-fire thermal differences are greatest (Hulley *et al.*, 2022). ECOSTRESS, in contrast, samples the land surface at varying local times because of the International Space Station orbit. This sampling pattern is analytically challenging because observations must be standardized for both season and time of day, but it also provides a rare opportunity to evaluate whether post-fire warming is concentrated during particular portions of the diurnal cycle. In fire-affected forests, this diurnal dimension may be critical for understanding plant stress, soil heating, atmospheric coupling, and the thermal environments associated with post-fire regeneration.

Surface thermal responses also occur within a biological context. Vegetation phenology is a sensitive indicator of climate, microclimate, disturbance, and recovery, because seasonal transitions in budbreak, leaf expansion, canopy development, and senescence integrate plant responses to environmental conditions. Vegetation growth phenology, comprising key biological events such as green-up and senescence, may shift as communities recover from fire (Van Leeuwen *et al.*, 2010; Wang & Zhang, 2020). These legacies also impact C and nutrient cycling (Kranabetter *et al.*, 2016; Lajtha & Jones, 2018), hydrology (Swanson *et al.*, 1998), and even the composition of biological communities (Dodds *et al.*, 2012; Frey *et al.*, 2016). Understanding these legacies is crucial to predict fire response and manage for resilience in a changing climate. Satellite vegetation indices can capture seasonal vegetation activity over large areas, but their ecological interpretation is not straightforward in structurally complex forests. Optical vegetation signals integrate canopy and understory layers, multiple species, shadows, sun-angle effects, disturbance legacies, and changes in vegetation cover. Long-term field phenology records are therefore essential for evaluating what remotely sensed phenology represents. The near-infrared reflectance of vegetation (NIRv) (Badgley *et al.*, 2019), derived from optical satellite reflectance, provides a useful measure of vegetation activity that can be compared with field-observed phenophases, especially when long time series are available.

The H.J. Andrews Experimental Forest (HJA) in the western Cascades of Oregon provides an exceptional setting for linking post-fire surface climate to vegetation phenology. HJA is a long-term ecological research landscape with steep environmental gradients, complex topography, diverse forest structure, extensive ecological monitoring, and long-term phenology observations. Its disturbance history includes wildfire, timber harvest, thinning, edge effects, and forest development across successional stages, producing a heterogeneous landscape in which post-fire responses are likely to depend on both current burn severity and pre-existing structure (Lutz & Halpern, 2006; Seidl *et al.*, 2014) (Bell *et al.*, 2017). At HJA, long-term field observations have shown that spring plant phenology is strongly shaped by local microclimate, snowpack, topography, and interannual climate variability, with warm, low-snow years reducing both microclimate and phenological diversity across the landscape (Ward *et al.*, 2018). The 2023 Lookout Fire burned across this landscape with variable severity, creating an opportunity to evaluate how a recent wildfire altered surface thermal regimes and vegetation activity in a well-instrumented forest ecosystem.

Here, we ask: How did the 2023 Lookout Fire alter the seasonal and diurnal surface thermal regime of the H.J. Andrews Experimental Forest, and how are these thermal changes linked to burn severity, forest structure, and vegetation phenology? We addressed this question by integrating ECOSTRESS LST, Harmonized Landsat–Sentinel-2 (HLS) NIRv, RAVG burn severity, Daymet climate, airborne LiDAR-derived forest structure and topography, and long-term field phenology observations from the HJA TV075 core phenology plots. We had five objectives: (1) quantify post-fire changes in ECOSTRESS LST across seasons, times of day, and burn-severity classes; (2) test whether burn severity, climate, and airborne LiDAR-derived structure and topography explain post-fire LST responses; (3) determine whether wildfire altered the coupling between ECOSTRESS LST and air temperature at core phenology plots; (4) evaluate how HLS NIRv relates to TV075 field phenology across plots, species, and years; and (5) link vegetation phenology and remotely sensed greenness to post-fire surface temperature. We expected post-fire warming to be strongest in high-severity burned areas, during summer daytime conditions, and in more open-canopy settings. We further expected HLS NIRv to capture broad seasonal and disturbance-related vegetation activity while showing plot- and species-specific relationships with field-observed phenology.

2. Materials and methods

2.1 Study area and 2023 Lookout Fire

The H.J. Andrews Experimental Forest is located in the Western Cascades of Oregon, USA, and encompasses steep topographic gradients, heterogeneous forest structure, and long-term ecological monitoring infrastructure. The site includes old-growth and second-growth forests, areas influenced by historical harvest and thinning, and long-term study plots that have been monitored for forest structure, climate, hydrology, vegetation dynamics, and phenology. This combination of complex terrain, heterogeneous disturbance history, and long-term ecological data makes HJA a useful landscape for evaluating how remotely sensed surface climate and vegetation phenology respond to wildfire.

The 2023 Lookout Fire began on 5 August 2023 and burned through late September 2023, affecting portions of the HJA landscape with variable burn severity (Figure 1). We used the Lookout Fire as a recent disturbance event to compare pre- and post-burn surface temperature and vegetation activity. Burn severity was represented using RAVG Composite Burn Index class 4 (CBI4), which classified pixels into unburned or unchanged areas and low-, moderate-, and high-severity burned areas. The spatial relationship among the HJA boundary, Lookout Fire perimeter, burn-severity classes, core phenology plots, topography, post-fire optical imagery, and summer ECOSTRESS LST is shown in Figure 1 (and Figures S1).

2.2 Overall analytical design

We used a two-pronged analytical design that a) the overlap of available remote sensing datasets and b) leveraged the HJA long-term ecological research context. First, we conducted a landscape-scale analysis of ECOSTRESS LST across stratified sampling cells distributed among burn-severity classes (Figure S2). This analysis was designed to quantify how pre- and post-burn surface temperature varied across seasons, times of day, burn severity, climate, forest structure, and topography. Second, we conducted targeted analyses at HJA core phenology plots, where satellite observations could be linked to long-term (TV075) field phenology (Schulze, 2023) and instantaneous air temperature observations (MS045) (Schulze *et al.*, 2026). This plot-level analysis allowed us to evaluate how remotely sensed vegetation activity and LST–air temperature coupling related to long-term ecological observations.

The landscape-scale ECOSTRESS sampling design included 450 cells stratified across RAVG CBI4 classes. We sampled 75 cells each from CBI4 classes 0 and 1 and 100 cells each from CBI4 classes 2, 3, and 4. Fewer cells were sampled from CBI4 0 and 1 because preliminary analyses indicated that unchanged and unburned areas were not distinguishable. The core phenology plot analysis focused on sites with long-term field phenology observations, HLS NIRv time series (Figure 2), ECOSTRESS LST observations, and local air temperature information. Together, these two spatial grains allowed us to evaluate broad landscape patterns while retaining ecological interpretation from long-term plot-level observations.

2.3 Remote sensing and environmental datasets

We integrated satellite, climate, and airborne LiDAR. ECOSTRESS LST was used to characterize land surface temperature across the HJA landscape and core phenology plots. ECOSTRESS TIR is processed to LST with the TES algorithm and multiple spectral band to simultaneous estimate emissivity and temperature (Hulley *et al.*, 2022). ECOSTRESS observations occur at varying local times and contain ISS processional error especially at higher latitudes. HLS surface reflectance was used to calculate NIRv for core phenology plots. NIRv was calculated from HLS near-infrared reflectance and NDVI as a remotely sensed measure of vegetation activity (Badgley *et al.*, 2019). We also calculated EVI, NDVI, CCI (Gamon *et al.*, 2016) and found that NIRv better captured seasonal patterns in preliminary testing. RAVG CBI4 burn-severity classes were used to define burn-severity groups and to model post-fire surface temperature responses.

Daymet climate variables were used to represent gridded meteorological conditions, including downwelling solar radiation (Srad), snow water equivalent (Swe), maximum air temperature (Tmax), vapor pressure (VP), and 30-day precipitation sum (Pcp) (Thornton *et al.*, 2020). Daymet was used rather than only local tower observations to support spatial generalization across the landscape and to reduce bias associated with proximity to individual meteorological stations. Airborne LiDAR-derived products were used to represent forest structure and topography, including digital terrain model elevation, canopy height (Figure S3), and open vegetation cover (calculated as percent vegetation shorter than 2 m). Field phenology data came from the HJA TV075 core phenology dataset, which includes species-level phenological observations at long-term plots. Instantaneous air temperature observations were used in core phenology plot analyses of LST–air temperature coupling. Multicollinearity among modeled covariates was evaluated before model fitting; variance inflation factors were less than 1.9 for all modeled variables.

2.4 ECOSTRESS LST preprocessing and quality control

We extracted ECOSTRESS LST observations to both landscape-scale sampling cells and core phenology plot locations. Observations were screened using ECOSTRESS quality information and then filtered for outliers. Outliers were identified within seasonal groupings using an interquartile range criterion: observations below $Q1 - 2.5 \times IQR$ or above $Q3 + 2.5 \times IQR$ were flagged and removed. This filter removed physically implausible or isolated extreme observations while retaining the expected seasonal structure of LST (Figure S4-5). Outlier screening, seasonal distributions after filtering, and time-of-day sampling patterns are shown in Figures S4–S6.

2.5 Harmonic standardization of ECOSTRESS LST

ECOSTRESS observations varied substantially across both day of year and time of day, requiring explicit standardization before comparing pre- and post-burn observations (Figure S6). We used harmonic regression to model seasonal and diurnal LST structure. Candidate models included seasonal harmonics of day of year, diurnal harmonics of time of day, seasonal × diurnal interactions, and site-specific diurnal random effects. Models were compared using and information theory approach and maximum likelihood (Table S1), and the selected model was refit using restricted maximum likelihood for final prediction and standardization.

The final harmonic model included seasonal harmonics, diurnal harmonics, their interaction, and a site-specific diurnal random slope. This model allowed LST observations to be standardized for seasonal and diurnal sampling differences (Figure S7), removed analysis aliasing from procession of the International Space Station orbit (Figure S8; e.g., a GAM fit could absorb variation at any time scale and so modeled time of day patterns would still include DOY, and vice versa), and provided the basis for subsequent comparisons of pre- and post-burn surface temperature.

2.6 Seasonal and diurnal post-fire LST analyses

We used standardized ECOSTRESS LST to evaluate seasonal and diurnal post-fire thermal regimes. First, we visualized LST in polar plots organized by day of year and time of day to compare severely burned and unburned areas before and after the Lookout Fire (Figure 3). Second, we calculated seasonal LST anomalies relative to pre-fire baseline conditions and summarized these anomalies by burn-severity class for winter, spring, summer, and fall (Figure 4; Figure S9). We modeled summer-standardized diurnal LST curves for post-burn burn-severity classes to evaluate how surface warming varied across the day. Finally, we compared ECOSTRESS observation timing with a typical Landsat thermal overpass time to evaluate whether fixed-overpass thermal observations would capture the strongest post-fire surface warming.

2.7 Pre- and post-burn mixed-effects analysis of LST

We fit mixed-effects models to test whether burn severity, climate, forest structure, and topography explained pre- and post-burn LST patterns. The response variable was ECOSTRESS LST, standardized as appropriate for seasonal and diurnal effects. Predictors included fire phase (pre-fire vs post-fire), burn severity, Daymet climate variables, and airborne LiDAR-derived structure and topography. Burn severity was represented both as continuous CBI for the continuous severity analysis and as RAVG CBI4 classes for planned contrasts. Climate predictors included Srad, VP, Pcp, and Tmax and Swe did not have variation in the summer. Structural and topographic predictors included canopy height, open vegetation cover, and digital terrain model elevation. Key interactions tested whether post-fire LST responses varied with burn severity and whether burn-severity effects were modified by climate (Figure 5-6). Additional interactions tested whether open vegetation cover modified climate sensitivity (Table

1). Table 1 reports selected contrasts and covariate effects intended to summarize the main pre- and post-burn mixed-effects results rather than every model coefficient. Candidate models were compared using AIC and likelihood ratio tests, and marginal and conditional R^2 (Table S2). Models included random effects for site or sampling cell and year and were fit with lme4 in R.

2.8 LST–air temperature coupling at core phenology plots

To test whether wildfire altered the coupling between surface temperature and atmospheric temperature (Still *et al.*, 2022), we fit a separate mixed-effects model at the core phenology plots. The response variable was ECOSTRESS LST (Figure 7). Predictors included instantaneous air temperature, fire phase, CBI4 burn-severity class, and their interactions, along with climate and structure covariates. The key interaction was instantaneous air temperature × CBI4 × fire phase, which tested whether the relationship between LST and air temperature changed after fire as a function of burn severity. Models included random effects for site and year. We also calculated ΔT as ECOSTRESS LST minus instantaneous air temperature and tested whether mean ΔT differed from zero using a one-sample t-test (Figure S10). Model-selection results are provided in Table S3.

2.9 HLS NIRv time series and field phenology

We extracted HLS reflectance observations to the HJA core phenology plots and applied cloud and quality screening. NIRv was calculated for each valid observation and used to generate plot-level time series from 2013 to 2025. These time series were compared with TV075 field phenology records (Schulze, 2023), with emphasis on Douglas-fir (*Pseudotsuga menziesii*; PSME) phenological stages including budbreak and leaf expansion. An example HLS NIRv time series with TV075 phenophase observations is shown in Figure 2, and NIRv time series across all core phenology plots are shown in Figure S11.

We evaluated phenological correspondence at multiple levels. First, we examined how field-observed phenophases aligned with seasonal NIRv curves within individual plots and years. Second, we compared species-level phenology with HJA-wide NIRv seasonality. Third, we evaluated whether plot-year NIRv metrics, including summer NIRv area under the curve and day of year of peak NIRv, were associated with field phenology and summer surface temperature. Supporting comparisons among NIRv, TV075 field phenology, species-specific phenology, and community-level phenological timing are provided in Figures S12–S15. Because HLS pixels integrate canopy, understory, species composition, shadows, and structural conditions, we interpreted NIRv as an integrated vegetation activity signal rather than as a direct measurement of any single species phenophase.

2.10 Linking vegetation phenology, NIRv, and surface temperature

We linked field phenology, HLS NIRv metrics, and ECOSTRESS LST at the core phenology plots. Specifically, we tested the relationship between summer HLS NIRv area under the curve and field-observed Douglas-fir budbreak. We also tested the relationship between the day of year of peak NIRv and noon-standardized summer ECOSTRESS LST. This simple approach focusing on summer temperatures was chosen after more commonly used fitting method were tried but were limited by the ’smile’ shaped pattern that causes many sites to have very high NIR reflectance in conifer forests in the winter (Kong *et al.*, 2022). These plot-year analyses were used to evaluate whether remotely sensed vegetation activity and field-observed phenological timing were associated with summer surface thermal conditions. These relationships are shown in Figure 8.

2.11 Landscape-scale relationships between vegetation activity and post-fire LST

To test whether post-fire changes in vegetation activity were associated with surface warming across the full stratified landscape sample, we modeled annual changes in noon-standardized land surface temperature (ΔLST; °C) for 888 site-year observations from 444 sites in 2024 and 2025. For each site and year, ΔLST was calculated as the difference between post-fire summer mean noon-standardized LST and the site-specific pre-fire summer mean. We used linear mixed-effects models with a site-level random intercept to account for repeated observations across post-fire years. Continuous predictors were standardized before model fitting. Candidate models included post-fire change in summer NIRv area under the curve (ΔNIRv AUC), burn severity, elevation, Daymet climate anomalies, absolute summer climate conditions, canopy openness, canopy height, and interactions between ΔNIRv AUC and climate. These analyses supported the landscape-scale vegetation–temperature relationships shown in Figure 9a and Figures S16–S19, with model selection and final model coefficients reported in Tables S4 and S5.

2.12 Structural Equation Modeling of evapotranspiration mediation of post-fire surface warming

To evaluate whether reduced evapotranspiration mediated the relationship between post-fire vegetation loss and daytime surface warming, we extracted ECOSTRESS Level-3 Tiled Joint ET daily evapotranspiration estimates for the same sites and years. Cloud- and water-contaminated pixels were removed using the product quality flags. For each site, summer ET anomalies (ΔET) were calculated as the difference between mean post-fire summer ET in 2024 or 2025 and the site-specific pre-fire summer mean. We then fit a piecewise structural equation model (Lefcheck, 2015) using two mixed-effects component models: one predicting ΔET from ΔNIRv AUC, burn severity, and elevation, and a second predicting ΔLST from ΔNIRv AUC, ΔET, burn severity, and elevation. Both component models included site-level random intercepts and standardized continuous predictors. Indirect effects were calculated using the product-of-coefficients approach. To evaluate the relative contributions of ET, vegetation activity, and burn severity to ΔLST independently of elevation (used to represent site level variation without overcomplicating the mediation model subset), we residualized variables against elevation-only mixed-effects models and used three-way variance partitioning. The resulting mediation structure is summarized in Figure 9b.

3. Results

3.1 Multi-sensor sampling captured burn-severity, structural, and phenology gradients

The Lookout Fire produced spatially heterogeneous burn severity across the H.J. Andrews Experimental Forest, creating a mosaic of unburned or unchanged, low-, moderate-, and high-severity areas (Figure 1a). Core phenology plots were distributed across this heterogeneous landscape and provided a link between remotely sensed surface temperature, remotely sensed vegetation activity, and long-term field observations. Summer 2025 ECOSTRESS LST showed strong spatial heterogeneity across the HJA extent (Figure 1b), while a June 2025 PlanetScope image illustrated post-fire variation in canopy condition, exposed surfaces, and vegetation recovery within and near the fire perimeter (Figure 1c). Together, these spatial datasets captured the intersection of burn severity, topographic complexity, forest structure, and field-observed phenology that underpinned the landscape-scale and core-plot analyses.

3.2 HLS NIRv captured long-term vegetation activity at core phenology plots

HLS NIRv time series captured strong seasonal and interannual variation in vegetation activity at core phenology plots. At the example plot PC009, NIRv showed repeated seasonal cycles from 2013 to 2025, with field-observed PSME phenophase dates occurring along the seasonal trajectory of remotely sensed greenness (Figure 2). Early phenophases such as bud swelling and budbreak occurred during the rising portion of the NIRv curve, whereas later leaf expansion and senescence phases aligned with later portions of the seasonal cycle. The time series also showed a pronounced decline in NIRv after the 2023 Lookout Fire, indicating that HLS NIRv was sensitive to post-fire canopy and surface change at affected plots. Across all core phenology plots, NIRv captured broad seasonal vegetation activity, disturbance signals, and site-level variation, while also showing that field phenology and satellite greenness are related but not interchangeable measures of plant activity (Figures S11–S15).

3.3 ECOSTRESS LST required seasonal and diurnal standardization

ECOSTRESS observations were distributed unevenly across both day of year and local time of day, reflecting the ISS orbit and making seasonal–diurnal standardization necessary before comparing pre- and post-burn LST. Quality screening and seasonal outlier filtering removed physically implausible observations while preserving the expected seasonal structure of LST (Figures S4 and S5). Observation timing varied across the seasonal cycle, confirming that unstandardized ECOSTRESS LST could confound seasonal and diurnal temperature variation if analyzed directly (Figure S6).

Harmonic model selection supported the inclusion of seasonal harmonics, diurnal harmonics, seasonal × diurnal interactions, and site-specific diurnal variation (Table S1). The final harmonic regression explained a large fraction of ECOSTRESS LST variation across the landscape, with marginal $R^2 = 0.77$ and conditional $R^2 = 0.78$. Model predictions showed that diurnal LST amplitude varied strongly across the year, with greater diurnal amplitude during summer and fall and weaker diurnal structure during winter (Figure S7). Standardized LST observations retained the expected seasonal signal while accounting for the timing of ECOSTRESS observations (Figure S8), providing the basis for subsequent pre- and post-burn comparisons. Overall, the harmonic regression successfully standardized the data such that the physical orbit and rotation of the earth with prescribed periods were accounted for while retaining biologically important residuals that contain variation theoretically related to energy balance, climate, fire, etc.

3.4 Post-fire LST divergence was strongest during summer

Seasonal–diurnal ECOSTRESS LST patterns differed strongly between severely burned and unburned areas after the Lookout Fire (Figure 3). In severely burned areas, post-fire LST diverged most strongly from the pre-fire reference pattern during the summer growing season, whereas unburned areas showed weaker post-fire departures. The polar representation of standardized LST highlighted that the post-fire thermal response was not uniform across the year; instead, the strongest differences occurred during the warm, high-radiation portion of the seasonal cycle.

Seasonal anomaly analyses confirmed that post-fire warming was concentrated during summer and increased with burn severity (Figure 4). High-severity burned areas showed the largest positive summer LST anomalies after the 2023 fire, whereas low-severity and unburned or unchanged areas showed weaker changes. Winter, spring, and fall responses were smaller or more variable, indicating that the Lookout Fire reorganized surface temperature most strongly under summer conditions. The underlying seasonal time series showed the same pattern, with post-fire divergence most apparent in summer and in higher-severity burn classes (Figure S9).

3.5 Burn severity, climate, and structure jointly controlled post-fire LST

The pre- and post-burn mixed-effects analysis showed that burn severity imposed a strong post-fire thermal effect after accounting for climate, forest structure, topography, site, and year. Pre-fire differences among eventual burn-severity classes were small and not statistically significant at $\alpha = 0.05$, indicating that the post-fire severity gradient was not simply a continuation of large pre-existing thermal differences among areas that later burned at different severities. After fire, however, LST increased strongly with burn severity (Figure 5). The continuous CBI relationship was weak before the Lookout Fire but strongly positive afterward, indicating that higher burn severity was associated with greater summer surface warming.

Planned contrasts from the pre- and post-burn mixed-effects model showed that high-severity burned areas were 1.47 ± 0.07 °C warmer than unburned or unchanged areas after fire ($p < 0.001$; Table 1). This high-severity warming was amplified under climate conditions associated with greater surface heating. The contrast between CBI4 class 4 and class 0 increased to 1.87 ± 0.09 °C at +1 SD solar radiation, 2.45 ± 0.14 °C at −1 SD 30-day precipitation, and 2.50 ± 0.11 °C at +1 SD vapor pressure (all $p < 0.001$; Table 1). Forest structure and topography also contributed to LST variation: open vegetation cover was associated with warmer LST (0.07 ±

0.02 °C per 1 SD increase, $p < 0.001$), whereas higher elevation was associated with cooler LST (−0.08 ± 0.02 °C per 1 SD increase, $p < 0.001$). The final landscape-scale mixed-effects model had marginal $R^2 = 0.309$ and conditional $R^2 = 0.362$, indicating that fixed effects captured substantial landscape-scale variation while random effects for site and year also contributed to model fit. Model-selection results supported the inclusion of fire–climate interactions in the landscape-scale model (Table S2). Slope and aspect were not retained in the models.

3.6 ECOSTRESS revealed diurnal post-fire warming that fixed-overpass sensors may miss

Summer diurnal LST curves showed that post-fire warming depended strongly on time of day (Figure 6a). Burned areas were warmer than unburned areas during daytime conditions, with the largest differences near midday and early afternoon. This diurnal pattern indicates that the magnitude of post-fire surface warming cannot be fully characterized from seasonal or daily mean patterns alone.

The seasonal–diurnal distribution of ECOSTRESS observations further showed why variable overpass time was important for this analysis (Figure 6b). ECOSTRESS sampled HJA across a broad range of local times, revealing high daytime LST observations that would not be captured by a single fixed overpass time. The typical Landsat thermal acquisition time occurred earlier than the period when post-fire surface warming was greatest, suggesting that fixed late-morning thermal observations may underestimate the magnitude of daytime post-fire heating. Thus, the same ISS sampling pattern that required harmonic standardization also provided a key advantage for resolving diurnal structure in the post-fire thermal regime.

3.7 Fire altered LST–air temperature coupling at core phenology plots

At core phenology plots, ECOSTRESS LST was strongly related to instantaneous air temperature, but this relationship changed after fire as a function of burn severity (Figure 7). Before the Lookout Fire, LST tracked air temperature closely across burn classes, with observations distributed near the 1:1 reference line. After fire, moderately burned plots showed a steeper LST–air temperature relationship, indicating stronger surface heating relative to air temperature under warmer atmospheric conditions.

The selected core phenology plot mixed-effects model was strongly supported relative to simpler models and explained most variation in LST, with marginal $R^2 = 0.88$ and conditional $R^2 = 0.89$ (Table S3). Instantaneous air temperature was the dominant predictor of LST (estimate = 1.04 ± 0.01, $p < 0.001$), but the air temperature × CBI4 × fire phase interaction was also significant (estimate = 0.0329 ± 0.01, $p = 0.004$), indicating that post-fire burn severity modified the coupling between LST and air temperature. Across core phenology plot observations, ECOSTRESS LST was generally warmer than instantaneous air temperature: mean ΔT was 0.55 °C, with a 95% confidence interval of 0.48 to 0.63 °C ($t = 13.8$, $df = 3680$, $p < 0.001$; Figure S10). These results show that wildfire altered not only mean surface temperature but also the relationship between surface temperature and atmospheric conditions at biologically monitored plots.

3.8 Vegetation phenology and NIRv metrics were linked to summer surface temperature

Field phenology, HLS NIRv, and ECOSTRESS LST were linked at the core phenology plots (Figure 8). Earlier field-observed Douglas-fir budbreak was associated with greater summer

NIRv area under the curve, indicating that earlier phenological activity corresponded to greater seasonal accumulation of remotely sensed vegetation activity (Figure 8a). The day of year of peak NIRv was also related to noon-standardized summer ECOSTRESS LST: plots and years with earlier peak NIRv tended to have warmer summer surface temperatures (Figure 8b). These relationships connect field-observed phenology, satellite-derived vegetation activity, and remotely sensed surface temperature.

The phenology analyses also showed important complexity in the interpretation of satellite greenness. Species-level field phenology spanned the seasonal NIRv green-up period, Douglas-fir phenophases aligned with different portions of the mean NIRv curve, and site-year curves showed that phenological stages occurred at broadly consistent positions within sites but varied among sites (Figures S12–S15). This pattern supports the interpretation that HLS NIRv captures integrated vegetation activity across canopy and understory layers rather than a one-to-one signal from individual species. In this context, the correspondence between NIRv, Douglas-fir budbreak, and summer LST provides evidence that remotely sensed vegetation activity can be used to place post-fire thermal change within a broader biological recovery framework.

3.9 Post-fire reduction in plant activity was associated with surface warming

Across the stratified landscape sample, summer vegetation activity declined after fire, with the largest reductions in high- and very-high-severity areas and smaller changes in unburned and moderate-severity areas (Figure S16). These changes corresponded to a shift toward lower NIRv AUC and higher predicted noon LST after fire, especially in high- and very-high-severity areas (Figure S17). When expressed as post-fire anomalies, larger reductions in summer NIRv AUC were generally associated with greater noon surface warming in both 2024 and 2025 (Figure 9a; Figure S18a,b). Daytime warming increased with burn severity, whereas nighttime LST generally declined across burn-severity classes (Figure S18c,d).

Model selection strongly supported the inclusion of climate, canopy, and ΔNIRv × climate terms (Table S4). The best-supported pruned interaction model retained ΔNIRv AUC × Tmax and ΔNIRv AUC × 30-day precipitation interactions, explained 63% of ΔLST variation with fixed effects alone, and explained 71% when site-level random effects were included. In this model, sites with larger reductions in NIRv AUC showed greater daytime warming ($\beta = -0.17 \pm 0.04$, $p < 0.001$), and warming increased with burn severity relative to unburned sites (moderate: $\beta = 0.24$; high: $\beta = 0.44$; very high: $\beta = 1.06$; all $p < 0.01$; Table S5). Warming was also greater in more open vegetation ($\beta = 0.15$, $p < 0.001$) and tended to be lower at higher elevations ($\beta = -0.13$, $p = 0.052$). The ΔNIRv–ΔLST relationship varied with climate: vegetation-loss-associated warming was strongest under cooler and drier absolute conditions and weakened under warmer or wetter conditions (Figure S19), indicating that post-fire vegetation loss and climate jointly structured daytime surface heating.

3.10 Evapotranspiration mediated the vegetation–surface temperature relationship

The structural equation model indicated that reductions in evapotranspiration explained most of the relationship between post-fire NIRv reduction and daytime surface warming (Figure 9b). Sites with larger declines in NIRv AUC also had larger declines in summer ET ($\beta = 0.36 \pm 0.04$, $p < 0.001$; $R^2m = 0.51$), and high- and very-high-severity sites showed significant ET reductions relative to unburned sites ($\beta = -0.23$ and -0.48 SD, respectively; both $p < 0.001$). In the LST component model, ΔET was the dominant predictor of daytime warming ($\beta = -0.65 \pm 0.03$, $p < 0.001$; $R^2m = 0.60$), whereas the direct path from ΔNIRv AUC to ΔLST was small and not significant after accounting for ΔET ($\beta = -0.03 \pm 0.04$, $p = 0.54$). Variance partitioning indicated that ΔET uniquely explained 32.1% of residual ΔLST variance, and ET-related variance accounted for 47.8% when shared fractions were included. In contrast, the unique direct burn-severity fraction explained 1.6% of residual ΔLST variance.

4. Discussion

4.1 Wildfire severity reorganized the post-fire surface thermal regime

The 2023 Lookout Fire produced a severity-dependent reorganization of surface temperature at HJA. We show that wildfire severity reorganized the surface energy balance by linking post-fire reduction in plant activity to warmer ECOSTRESS land surface temperatures, primarily through reduced latent heat flux rather than through radiative surface change alone. Post-fire warming was strongest in high-severity burned areas, concentrated during summer, and most evident during daytime conditions. This pattern is consistent with the expectation that canopy loss and surface exposure alter the surface energy balance by increasing solar radiation reaching the ground and reducing any buffering capacity of intact forest canopies. The seasonal specificity of the response is important. The strongest fire effect occurred during the period when radiation load, atmospheric water demand, and ecological sensitivity to heat and water stress are likely to be greatest. In contrast, winter, spring, and fall responses were weaker or more variable, suggesting that post-fire thermal impacts cannot be inferred from annual averages or from burned/unburned contrasts alone.

The strong post-fire relationship between burn severity and summer LST indicates that severity is a key organizing axis for post-fire surface climate. Areas that ultimately burned at different severities did not show large pre-fire thermal differences, but after the Lookout Fire, high-severity areas were substantially warmer than unburned or unchanged areas. This supports the interpretation that the fire produced a new thermal gradient across the landscape. Importantly, the magnitude of this gradient depended on environmental conditions: high-severity warming was amplified under high solar radiation, drier antecedent conditions, and higher vapor pressure. These interactions suggest that post-fire surface warming will be most pronounced during the same climate conditions that are relevant to plant stress, regeneration constraints, and future fire risk.

4.2 Diurnal sampling is central to interpreting post-fire LST

A major contribution of this study is showing that the post-fire thermal response was diurnally structured. Burned areas were not simply warmer in a mean sense; they were especially warmer during daytime conditions near midday and early afternoon. This distinction matters because ecological exposure to heat is time-dependent. Plant tissues, seedlings, soils, and near-surface organisms may experience the strongest thermal stress during the warmest portions of the day, and these conditions may not be represented by fixed-overpass observations.

ECOSTRESS was critical because its variable ISS overpass time allowed us to observe the seasonal–diurnal structure of LST, adding to the literature that demonstrate this value for biology and ecology (Gustine *et al.*, 2023; Holzmann *et al.*, 2026; Pérez-Planells *et al.*, 2026). Although this sampling pattern required harmonic standardization, it revealed high daytime post-fire LST that a fixed late-morning overpass would likely miss. This has broader implications for post-fire remote sensing. Long-term fixed-overpass thermal records remain essential for trend analysis, but they may underestimate the magnitude of post-fire thermal exposure if peak heating occurs outside the overpass window. ECOSTRESS therefore provides a complementary perspective by resolving how disturbance effects vary across the diurnal cycle.

4.3 Forest structure, topography, and climate mediated post-fire warming

Post-fire LST responses were shaped not only by burn severity but also by forest structure, topography, and climate. Airborne LiDAR-derived open vegetation cover was associated with warmer LST, whereas higher elevations were cooler after accounting for other predictors. These relationships are consistent with the role of canopy structure and terrain in regulating surface energy balance. More open vegetation likely increases exposure to direct radiation and reduces canopy buffering, while elevation integrates multiple climatic and topographic gradients that can influence temperature, moisture, snow persistence, and forest composition.

The open-cover and climate interactions further indicate that post-fire surface temperature emerges from multiple interacting drivers rather than a single fire-severity effect. Recent precipitation was associated with lower LST in more open vegetation, while vapor pressure was associated with greater LST in more open vegetation. These model-adjusted relationships should be interpreted cautiously because climate variables are correlated components of the surface energy and water-balance environment. Nevertheless, they reinforce the central finding that post-fire warming is conditional and the thermal consequences of burn severity depend on the weather and structural context in which burned surfaces are observed.

4.4 Fire modified the coupling between land surface temperature and air temperature

At core phenology plots, LST was strongly coupled to instantaneous air temperature, but the nature of this coupling changed after fire. Before the Lookout Fire, LST tracked air temperature similarly across burn classes. After fire, moderately burned areas showed a steeper LST–air temperature relationship, indicating that surface temperatures in burned plots increased more strongly with atmospheric warming. The positive mean ΔT further showed that ECOSTRESS LST was generally warmer than air temperature across observations. This results has important implications for the ability of ecosystems to respond to increasing temperatures and atmospheric drought (Kim *et al.*, 2016, 2018; Pau *et al.*, 2018; Still *et al.*, 2022).

This result highlights why air temperature alone may be insufficient for characterizing post-fire thermal environments. Air temperature is often the most available and widely used climate variable in ecological analyses, but surface temperature integrates radiation, canopy structure, moisture, and surface properties in ways that can diverge from air temperature. In burned forests, where canopy buffering is reduced and exposed surfaces are more common, this divergence may become ecologically important. Direct thermal remote sensing therefore provides information about the surface environments experienced by vegetation, soils, and regenerating plants that is not fully captured by air temperature records.

4.5 Phenology provides biological context for post-fire thermal change

Our results extend prior HJA field studies showing that microclimate heterogeneity structures spring phenology across the western Cascades (Ward *et al.*, 2018) by linking phenological variation to satellite-derived vegetation activity and post-fire surface thermal regimes. HLS NIRv and TV075 field phenology provided the biological layer needed to interpret post-fire surface climate change. NIRv captured strong seasonal cycles, interannual variation, and disturbance effects at core phenology plots, including declines following recent fire impacts. Field phenology observations showed how species-level phenophases aligned with the seasonal trajectory of remotely sensed greenness. These comparisons demonstrate that HLS NIRv is an ecologically meaningful measure of vegetation activity at HJA, but also that it should be interpreted as an integrated canopy and community signal rather than as a direct proxy for any single species or phenophase.

The relationship between Douglas-fir budbreak and summer NIRv accumulation indicates that field-observed phenology is linked to seasonal vegetation activity measured from space. The association between earlier peak NIRv and warmer summer LST further suggests that surface thermal conditions and vegetation phenology are coupled across the core phenology plots. These results do not imply a simple causal pathway in which warmer surfaces universally accelerate phenology. Instead, they indicate that post-fire surface climate and vegetation activity are linked components of ecosystem response, shaped by site conditions, species composition, canopy structure, and disturbance history.

The landscape-scale change analysis strengthens this interpretation by showing that NIRv was not only a phenological or greenness metric, but also a functional indicator of post-fire surface energy exchange. Across the stratified sample, declines in summer NIRv were associated with warmer noon-standardized LST, and the SEM indicated that this relationship was largely mediated by reductions in ECOSTRESS evapotranspiration. Thus, the biological signal captured by HLS NIRv appears to be linked to surface warming through the loss of evaporative cooling, while retained direct effects of burn severity suggest additional contributions from physical changes to the post-fire surface. This coupling among vegetation activity, evapotranspiration, and LST provides a mechanistic bridge between remotely sensed phenology and the severity-dependent thermal response observed after the Lookout Fire.

4.6 Implications for post-fire monitoring in long-term ecological research landscapes

This study illustrates the value of integrating multi-sensor remote sensing with long-term ecological observations. ECOSTRESS provided the diurnal thermal dimension, HLS provided seasonal vegetation activity, RAVG provided burn-severity context, Daymet provided spatially continuous climate covariates, and airborne LiDAR provided structural and topographic information. The HJA TV075 phenology records anchored the optical time series in field-observed plant phenology, allowing remotely sensed greenness to be interpreted in relation to specific phenological stages and plot-level ecological variation.

Long-term research landscapes such as HJA are particularly valuable for this type of integration because they provide the field context needed to interpret satellite signals after disturbance. Fire perimeters and burn-severity maps are essential, but they do not fully capture how disturbance reorganizes microclimate, vegetation activity, and biological recovery. By linking surface temperature, structure, climate, and phenology, this approach provides a framework for monitoring post-fire ecosystems in ways that are both spatially extensive and ecologically grounded.

4.7 Limitations and future directions

Several limitations should be considered. First, the post-fire record remains short, and continued observations will be needed to determine whether the observed surface warming persists, declines with vegetation recovery, or changes as post-fire communities develop. Second, ECOSTRESS sampling is irregular in space and time. Harmonic/Fourrier standardization addresses the dominant seasonal and diurnal structure, but uneven observation timing remains an inherent feature of the dataset. Third, HLS NIRv can be influenced by snow, shadows, sun angle, mixed canopy and understory signals, and post-fire changes in surface background. These factors are particularly important in steep, structurally complex forests, and perhaps a SWIR based metric would provide and improvement . Fourth, field phenology observations are species-specific, whereas HLS pixels integrate vegetation across species and canopy layers. This mismatch is a central reason to interpret NIRv as an integrated vegetation activity signal rather than as a direct phenophase measurement. Finally, bBecause vegetation activity and surface temperature likely influence one another, our SEM focused on the most direct hypothesized pathway from post-fire vegetation loss to reduced evapotranspiration and warmer LST, rather than attempting to fully resolve bidirectional feedbacks between NIRv and surface temperature which was not within our scope.

The landscape-scale change models extend the plot-level phenology results by showing that post-fire surface warming was coupled to vegetation loss across the full stratified sample. Sites with larger reductions in summer NIRv AUC showed greater increases in noon-standardized LST, particularly in high- and very-high-severity areas, indicating that the thermal consequences of fire were linked not only to burn severity but also to the loss of seasonally integrated vegetation activity. The climate interactions suggest that this vegetation–temperature coupling was conditional on the post-fire atmospheric environment, with the strongest greenness-loss warming under cooler and drier absolute conditions and weaker coupling under warmer or wetter conditions. The structural equation model provides a mechanistic interpretation of this pattern: once ECOSTRESS evapotranspiration was included, the direct path from NIRv loss to LST was small and non-significant, whereas reduced ET was strongly associated with warmer daytime surfaces. This result is consistent with a dominant latent-heat-flux pathway, in which fire-driven reductions in vegetation activity reduce evaporative cooling and thereby increase daytime surface temperature. At the same time, the retained direct effects of burn severity indicate that physical changes to the post-fire surface, including canopy opening, altered albedo, soil exposure, and changes in radiation absorption, likely contribute additional warming beyond what is captured by NIRv and ET alone.

Future work can extend this analysis as additional post-fire years become available, allowing stronger tests of recovery trajectories and phenological change through time. Repeat LiDAR after fire would improve the ability to attribute thermal changes directly to canopy loss and structural recovery. Additional field microclimate sensors and thermal camera observations could further evaluate how ECOSTRESS LST relates to canopy, understory, and near-surface thermal environments. Future work could also include evapotranspiration estimates. HJA phenocam images will be analyzed for phenological indicators like greenness (i.e., Sonnentag *et* *al.*, 2012). Opportunities exist to connect the thermal responses to habitat modeling (Wolf *et al.*, 2021; Kim *et al.*, 2022). Finally, applying the same framework to other western Cascade fires would test whether the severity-dependent and diurnally structured warming observed at HJA is general across similar forest landscapes.

5. Conclusions

The 2023 Lookout Fire produced a severity-dependent reorganization of the surface thermal regime at the H.J. Andrews Experimental Forest. Post-fire warming was strongest during summer daytime conditions and was mediated by burn severity, climate, canopy openness, and topography. ECOSTRESS was essential for detecting the diurnal structure of this response, revealing post-fire surface heating that fixed-overpass thermal observations may not fully capture. At core phenology plots, wildfire altered the coupling between LST and air temperature, showing that surface thermal environments can diverge from atmospheric temperature after disturbance. HLS NIRv and TV075 field phenology provided the biological context for these thermal changes, linking remotely sensed vegetation activity and phenological timing to summer surface temperature. The role of NIRv in surface temperature changes was mediated through laten heat flux. Together, these results show that wildfire effects on forest ecosystems are not captured by fire perimeter alone; they emerge from interactions among burn severity, structure, climate, topography, and vegetation phenology. Multi-sensor remote sensing anchored by long-term ecological observations provides a powerful framework for quantifying these coupled physical and biological responses to disturbance.

Declaration of competing interest

The authors declare that they have no known competing financial interests or personal relationships that could have appeared to influence the work reported in this paper.

Acknowledgements

DMG was supported by NSF Award 2550974 and by NSF grant LTER8 DEB-2025755. Data were provided by the H.J. Andrews Experimental Forest and Long Term Ecological Research (LTER) program, administered cooperatively by Oregon State University, the USDA Forest Service Pacific Northwest Research Station, and the Willamette National Forest. This material is based upon work supported by the National Science Foundation under the grant LTER8 DEB-2025755

Data availability

A code repository will be shared

Modeled surface temperature products will be archived in the Forest Science Data Bank

Publicly available datasets, including ECOSTRESS, HLS, RAVG, and Daymet products, will be referenced directly.

References

Badgley G, Anderegg LDL, Berry JA, Field CB. **2019**. Terrestrial gross primary production: Using NIR_V to scale from site to globe. *Global Change Biology* **25**: 3731–3740.

Bell DM, Spies TA, Pabst R. **2017**. Historical harvests reduce neighboring old-growth basal area across a forest landscape. *Ecological Applications* **27**: 1666–1676.

Busby SU, Klock AM, Fried JS. **2023**. Inventory analysis of fire effects wrought by wind-driven megafires in relation to weather and pre-fire forest structure in the western Cascades. *Fire Ecology* **19**: 58.

Chen J, Franklin JF, Spies TA. **1992**. Vegetation Responses to Edge Environments in Old-Growth Douglas-Fir Forests. *Ecological Applications* **2**: 387–396.

Chen J, Saunders SC, Crow TR, Naiman RJ, Brosofske KD, Mroz GD, Brookshire BL, Franklin JF. **1999**. Microclimate in Forest Ecosystem and Landscape Ecology. *BioScience* **49**: 288–297.

Dodds WK, Robinson CT, Gaiser EE, Hansen GJA, Powell H, Smith JM, Morse NB, Johnson SL, Gregory SV, Bell T, *et al.* **2012**. Surprises and Insights from Long-Term Aquatic Data Sets and Experiments. *BioScience* **62**: 709–721.

Frey SJK, Hadley AS, Betts MG. **2016**. Microclimate predicts within-season distribution dynamics of montane forest birds (M Robertson, Ed.). *Diversity and Distributions* **22**: 944–959.

Gamon JA, Huemmrich KF, Wong CYS, Ensminger I, Garrity S, Hollinger DY, Noormets A, Peñuelas J. **2016**. A remotely sensed pigment index reveals photosynthetic phenology in evergreen conifers. *Proceedings of the National Academy of Sciences* **113**: 13087–13092.

Gosnell H, Kennedy R, Harris T, Abrams J. **2020**. A land systems science approach to assessing forest governance and characterizing the emergence of social forestry in the Western Cascades of Oregon. *Environmental Research Letters* **15**: 055003.

Gustine RN, Nickles CL, Lee CM, Crawford BA, Hestir EL, Khanna S. **2023**. Evaluating Habitat Suitability and Tidal Wetland Restoration Actions With ECOSTRESS. *Journal of Geophysical Research: Biogeosciences* **128**: e2022JG007306.

Halofsky JS, Conklin DR, Donato DC, Halofsky JE, Kim JB. **2018**. Climate change, wildfire, and vegetation shifts in a high-inertia forest landscape: Western Washington, U.S.A. (C Carcaillet, Ed.). *PLOS ONE* **13**: e0209490.

Halofsky JE, Peterson DL, Harvey BJ. **2020**. Changing wildfire, changing forests: the effects of climate change on fire regimes and vegetation in the Pacific Northwest, USA. *Fire Ecology* **16**: 4.

Holzmann KL, Schmitzer T, Abels A, Čorkalo M, Mitesser O, Kortmann M, Alonso-Alonso P, Correa-Carmona Y, Pinos A, Yon F, *et al.* **2026**. Limited thermal tolerance in tropical insects and its genomic signature. *Nature* **651**: 672–678.

Hulley GC, Gottsche FM, Rivera G, Hook SJ, Freepartner RJ, Martin MA, Cawse-Nicholson K, Johnson WR. **2022**. Validation and Quality Assessment of the ECOSTRESS Level-2 Land Surface Temperature and Emissivity Product. *IEEE Transactions on Geoscience and Remote Sensing* **60**: 1–23.

Kim H, McComb BC, Frey SJK, Bell DM, Betts MG. **2022**. Forest microclimate and composition mediate long-term trends of breeding bird populations. *Global Change Biology* **28**: 6180–6193.

Kim Y, Still CJ, Hanson CV, Kwon H, Greer BT, Law BE. **2016**. Canopy skin temperature variations in relation to climate, soil temperature, and carbon flux at a ponderosa pine forest in central Oregon. *Agricultural and Forest Meteorology* **226–227**: 161–173.

Kim Y, Still CJ, Roberts DA, Goulden ML. **2018**. Thermal infrared imaging of conifer leaf temperatures: Comparison to thermocouple measurements and assessment of environmental influences. *Agricultural and Forest Meteorology* **248**: 361–371.

Kong D, McVicar TR, Xiao M, Zhang Y, Peña-Arancibia JL, Filippa G, Xie Y, Gu X. **2022**. *phenofit* : An R package for extracting vegetation phenology from time series remote sensing. *Methods in Ecology and Evolution* **13**: 1508–1527.

Kranabetter JM, McLauchlan KK, Enders SK, Fraterrigo JM, Higuera PE, Morris JL, Rastetter EB, Barnes R, Buma B, Gavin DG, *et al.* **2016**. A Framework to Assess Biogeochemical Response to Ecosystem Disturbance Using Nutrient Partitioning Ratios. *Ecosystems* **19**: 387–395.

Lajtha K, Jones J. **2018**. Forest harvest legacies control dissolved organic carbon export in small watersheds, western Oregon. *Biogeochemistry* **140**: 299–315.

Lefcheck JS. **2015**. piecewiseSEM: Piecewise structural equation modeling in R for ecology, evolution, and systematics. *Methods in Ecology and Evolution*: n/a-n/a.

Lutz JA, Halpern CB. **2006**. TREE MORTALITY DURING EARLY FOREST DEVELOPMENT: A LONG-TERM STUDY OF RATES, CAUSES, AND CONSEQUENCES. *Ecological Monographs* **76**: 257–275.

Pau S, Detto M, Kim Y, Still CJ. **2018**. Tropical forest temperature thresholds for gross primary productivity. *Ecosphere* **9**: e02311.

Pérez-Planells L, Göttsche F-M, Cermak J. **2026**. Annual and diurnal temperature cycle modelling of a merged multi-annual ECOSTRESS and Landsat land surface temperature dataset. *International Journal of Applied Earth Observation and Geoinformation* **149**: 105276.

Sánchez J, Bisquert M, Rubio E, Caselles V. **2015**. Impact of Land Cover Change Induced by a Fire Event on the Surface Energy Fluxes Derived from Remote Sensing. *Remote Sensing* **7**: 14899–14915.

Schulze MD. **2023**. Vegetative Phenology observations at the Andrews Experimental Forest, 2009 - Present.

Schulze MD, Betts MG, Frey SJK. **2026**. Air temperature at core phenology sites and additional bird monitoring sites in the Andrews Experimental Forest, 2009 to present.

Seidl R, Rammer W, Spies TA. **2014**. Disturbance legacies increase the resilience of forest ecosystem structure, composition, and functioning. *Ecological Applications* **24**: 2063–2077.

Sonnentag O, Hufkens K, Teshera-Sterne C, Young AM, Friedl M, Braswell BH, Milliman T, O'Keefe J, Richardson AD. **2012**. Digital repeat photography for phenological research in forest ecosystems. *Agricultural and Forest Meteorology* **152**: 159–177.

Still CJ, Page G, Rastogi B, Griffith DM, Aubrecht DM, Kim Y, Burns SP, Hanson CV, Kwon H, Hawkins L, *et al.* 2022. No evidence of canopy-scale leaf thermoregulation to cool leaves below air temperature across a range of forest ecosystems. *Proceedings of the National Academy of Sciences* **119**: e2205682119.

Still C, Powell R, Aubrecht D, Kim Y, Helliker B, Roberts D, Richardson AD, Goulden M. **2019**. Thermal imaging in plant and ecosystem ecology: applications and challenges. *Ecosphere* **10**.

Still CJ, Rastogi B, Page GFM, Griffith DM, Sibley A, Schulze M, Hawkins L, Pau S, Detto M, Helliker BR. **2021**. Imaging canopy temperature: shedding (thermal) light on ecosystem processes. *New Phytologist* **230**: 1746–1753.

Swanson FJ, Johnson SL, Gregory SV, Acker SA. **1998**. Flood Disturbance in a Forested Mountain Landscape. *BioScience* **48**: 681–689.

Tepley AJ, Thomann E, Veblen TT, Perry GLW, Holz A, Paritsis J, Kitzberger T, Anderson-Teixeira KJ. **2018**. Influences of fire–vegetation feedbacks and post-fire recovery rates on forest landscape vulnerability to altered fire regimes (E Lines, Ed.). *Journal of Ecology* **106**: 1925–1940.

Thornton MM, Shrestha R, Wei Y, Thornton PE, Kao S-C. **2020**. DaymetDaymet: Daily Surface Weather Data on a 1-km Grid for North America, Version 4. : 0 MB.

Van Leeuwen WJD, Casady GM, Neary DG, Bautista S, Alloza JA, Carmel Y, Wittenberg L, Malkinson D, Orr BJ. **2010**. Monitoring post-wildfire vegetation response with remotely sensed time-series data in Spain, USA and Israel. *International Journal of Wildland Fire* **19**: 75.

Wang J, Zhang X. **2020**. Investigation of wildfire impacts on land surface phenology from MODIS time series in the western US forests. *ISPRS Journal of Photogrammetry and Remote Sensing* **159**: 281–295.

Ward SE, Schulze M, Roy B. **2018**. A long-term perspective on microclimate and spring plant phenology in the Western Cascades. *Ecosphere* **9**: e02451.

Wasserman TN, Mueller SE. **2023**. Climate influences on future fire severity: a synthesis of climate-fire interactions and impacts on fire regimes, high-severity fire, and forests in the western United States. *Fire Ecology* **19**: 43.

Wolf C, Bell DM, Kim H, Nelson MP, Schulze M, Betts MG. **2021**. Temporal consistency of undercanopy thermal refugia in old-growth forest. *Agricultural and Forest Meteorology* **307**: 108520.

Tables

Table 1. Planned contrasts and covariate effects from the pre- and post-fire mixed effects model of land surface temperature. Estimates are in °C. Continuous covariates were standardized; therefore, covariate effects represent the expected change in land surface temperature (LST) per 1 SD increase in the predictor, conditional on the rest of the model. For conditional burn-severity contrasts, the covariate condition is shown after "|". Pre-fire contrasts among eventual burn-severity classes were small and not statistically significant at $\alpha = 0.05$.. Srad is downwelling solar radiation, VP is water vapor pressure, Pcp is 30-day precipitation sum, and Tmax is maximum air temperature. Climate data are from Daymet, and forest structure and elevation data are from airborne LiDAR. Model selection information is provided in Supplemental Table SX.

Model component	**Contrast or effect**	**Estimate ± SE (°C)**	**p**	**Description**
Burn-severity post-fire effect	CBI 4 - 0	1.47 ± 0.07	<0.001	High-severity areas showed the strongest additional post-fire warming.
Climate modification of burn-severity warming	CBI 4 – 0 | + 1 SD Srad	1.87 ± 0.09	<0.001	High-severity warming increased under higher solar radiation.
	CBI 4 – 0 | - 1 SD Pcp	2.45 ± 0.14	<0.001	High-severity warming was reduced following wetter periods and increased in dry periods.
	CBI 4 – 0 | + 1 SD VP	2.50 ± 0.11	<0.001	High-severity warming increased with higher vapor pressure
Forest structure and topography	Open vegetation cover	0.07 ± 0.02	<0.001	More open vegetation cover was associated with warmer LST.
	Digital terrain model elevation	−0.08 ± 0.02	<0.001	Higher-elevation areas were cooler.
	Open cover × Pcp	−0.05 ± 0.01	<0.001	Recent precipitation associated with lower LST in more open vegetation
	Open cover × VP	0.06 ± 0.01	<0.001	Vapor pressure was associated with greater LST in more open vegetation.
	Open cover × Tmax	−0.07 ± 0.02	<0.001	Open vegetation showed weaker LST sensitivity to maximum air temperature after accounting for other variables.

Figures

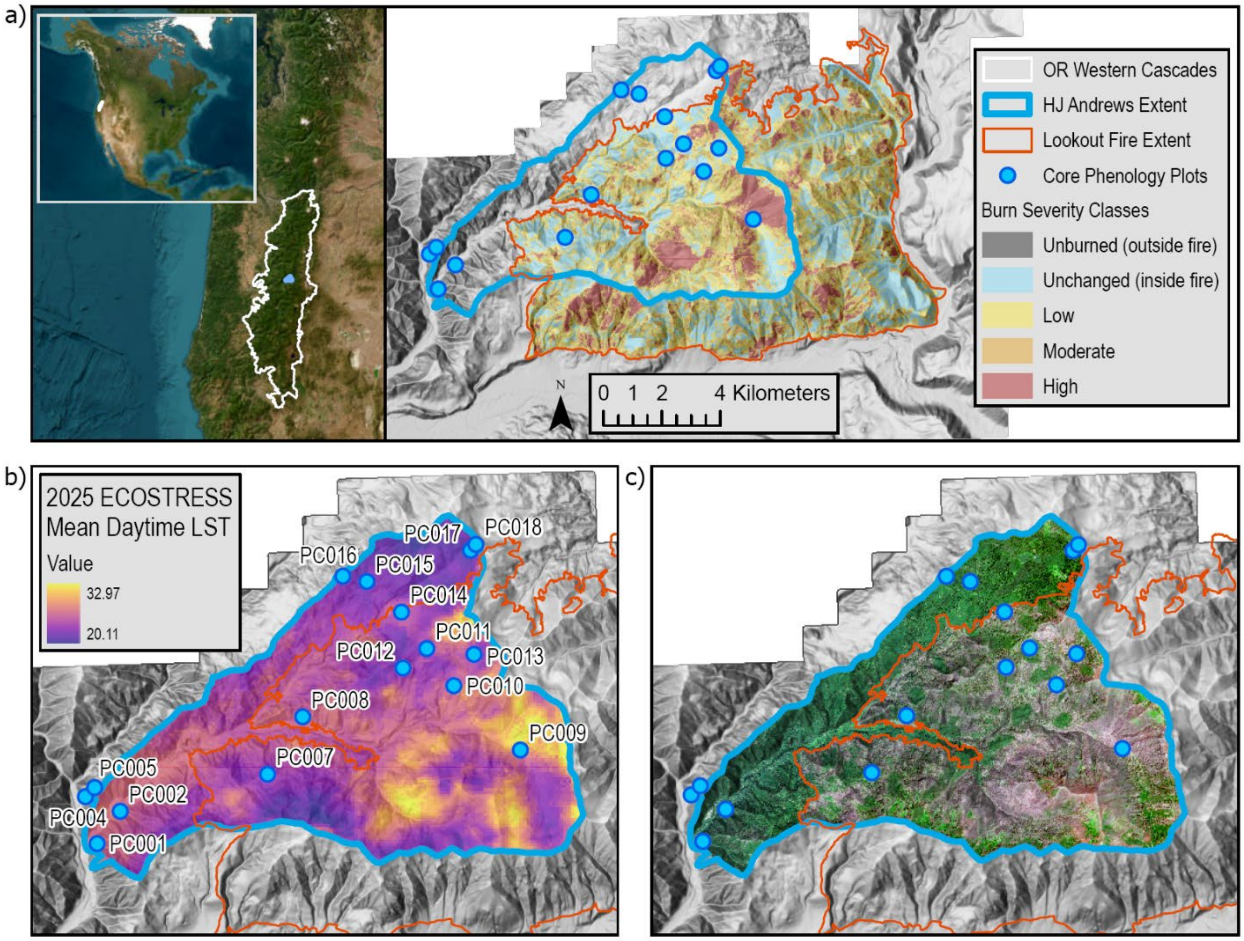

Figure 1. Study region, burn severity, and remote sensing context for the Lookout Fire at the H.J. Andrews Experimental Forest. (a) Location of the H.J. Andrews Experimental Forest in the Western Cascades of Oregon, showing the HJA boundary, Lookout Fire (Aug 5 - ~ Sept 30 2023) perimeter, core phenology plots, and burn-severity classes. Burn severity is shown for unburned areas outside the fire perimeter and the RAVG CBI4 classes: (1) unchanged pixels within the fire perimeter, and (2) low-, (3) moderate-, and (4) high-severity burned areas. (b) Mean daytime ECOSTRESS land surface temperature (LST) in summer 2025 across the HJA extent, with core phenology plots labeled. (c) Post-fire Planet Scope (3 m) optical image from June 24, 2025, showing the spatial heterogeneity of canopy loss and vegetation condition within the HJA boundary and Lookout Fire perimeter. Together, these panels show the spatial relationship among topography (airborne 1m LiDAR DTM), burn severity, phenology monitoring locations, and remotely sensed surface temperature.

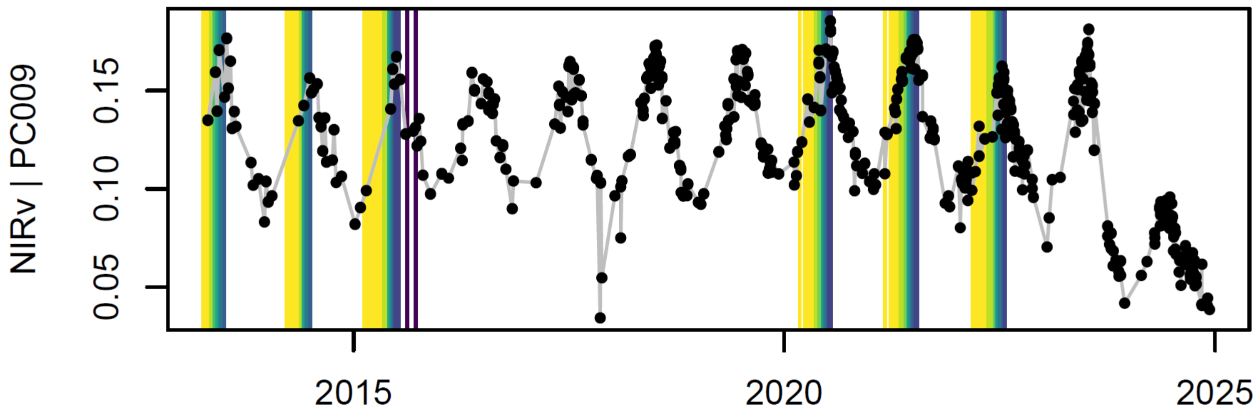

Figure 2. Harmonized Landsat–Sentinel-2 NIRv time series for an example core phenology plot. Time series of near-infrared reflectance of vegetation (NIRv) for plot PC009 from 2013 to 2025, derived from Harmonized Landsat–Sentinel-2 observations. Points show individual cloud- and quality-screened observations. Colored vertical bands indicate field-observed PSME phenophase dates (TV075) used to compare remotely sensed vegetation dynamics with long-term HJA phenology records (from swelling of buds and budbreak in yellow shades to full leaf expansion and leaf senescence in green and blue shades, respectively). The decline in NIRv after the 2023 Lookout Fire illustrates the sensitivity of the satellite vegetation signal to post-fire canopy and surface change.

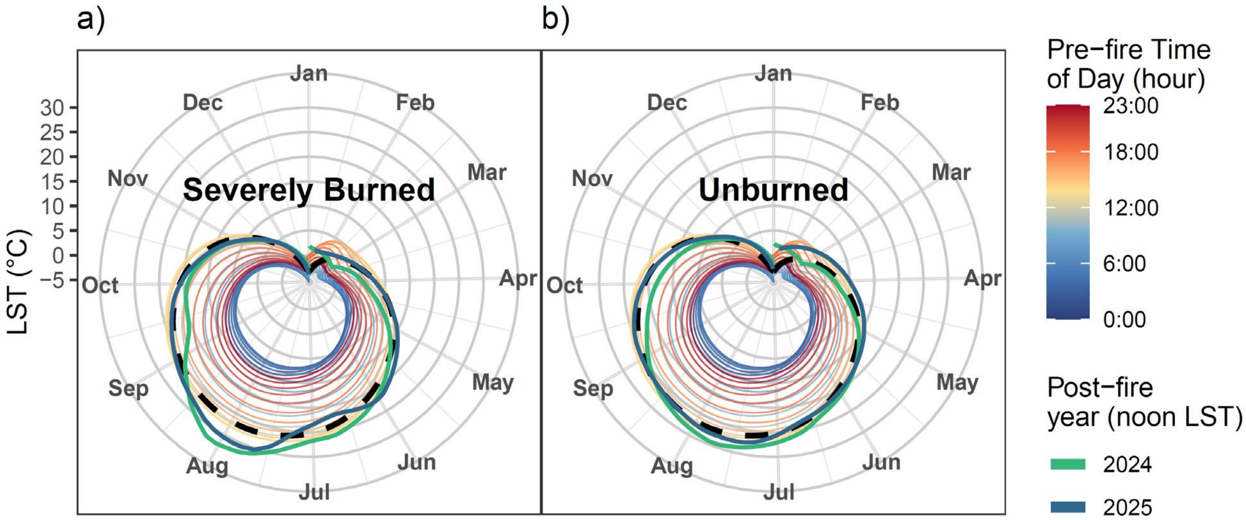

Figure 3. Seasonal and diurnal ECOSTRESS land surface temperature regimes before and after the Lookout Fire. Polar plots show ECOSTRESS LST, standardized by harmonic regression across day of year and time of day for pre-fire baseline conditions (dark blue to dark orange color scale) and loess curves for individual post burn years (noon standardized). LST is shown in (a) severely burned and (b) unburned areas to illustrate the continuing thermal impact of the Lookout Fire primarily on summer conditions. The black dashed curve indicates the pre-fire noon reference pattern for direct comparison. Comparing burned and unburned areas highlights how post-fire surface temperature regimes diverged most strongly during the summer growing season.

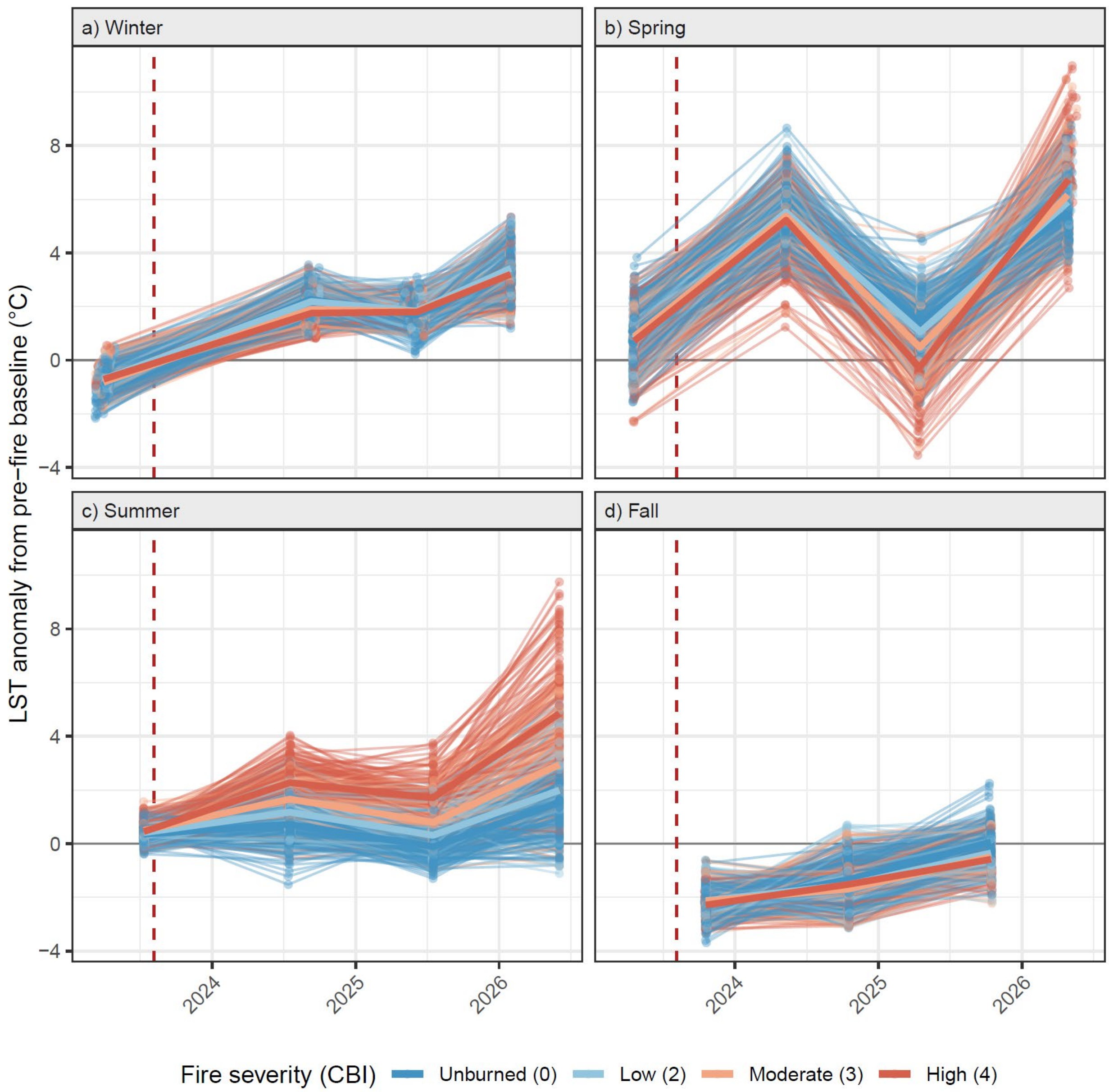

Figure 4. Seasonal LST anomalies after the Lookout Fire by burn-severity class. Land surface temperature anomalies are shown relative to the pre-fire baseline for (a) winter, (b) spring, (c) summer, and (d) fall. Points and thin lines show ECOSTRESS cell-level trajectories, and thick lines show class-level trends for unburned/unchanged, low-, moderate-, and high-severity burn classes. The dashed vertical line marks the timing of the 2023 Lookout Fire. Post-fire warming was strongest during summer and increased with burn severity, whereas seasonal responses were weaker or more variable in winter, spring, and fall.

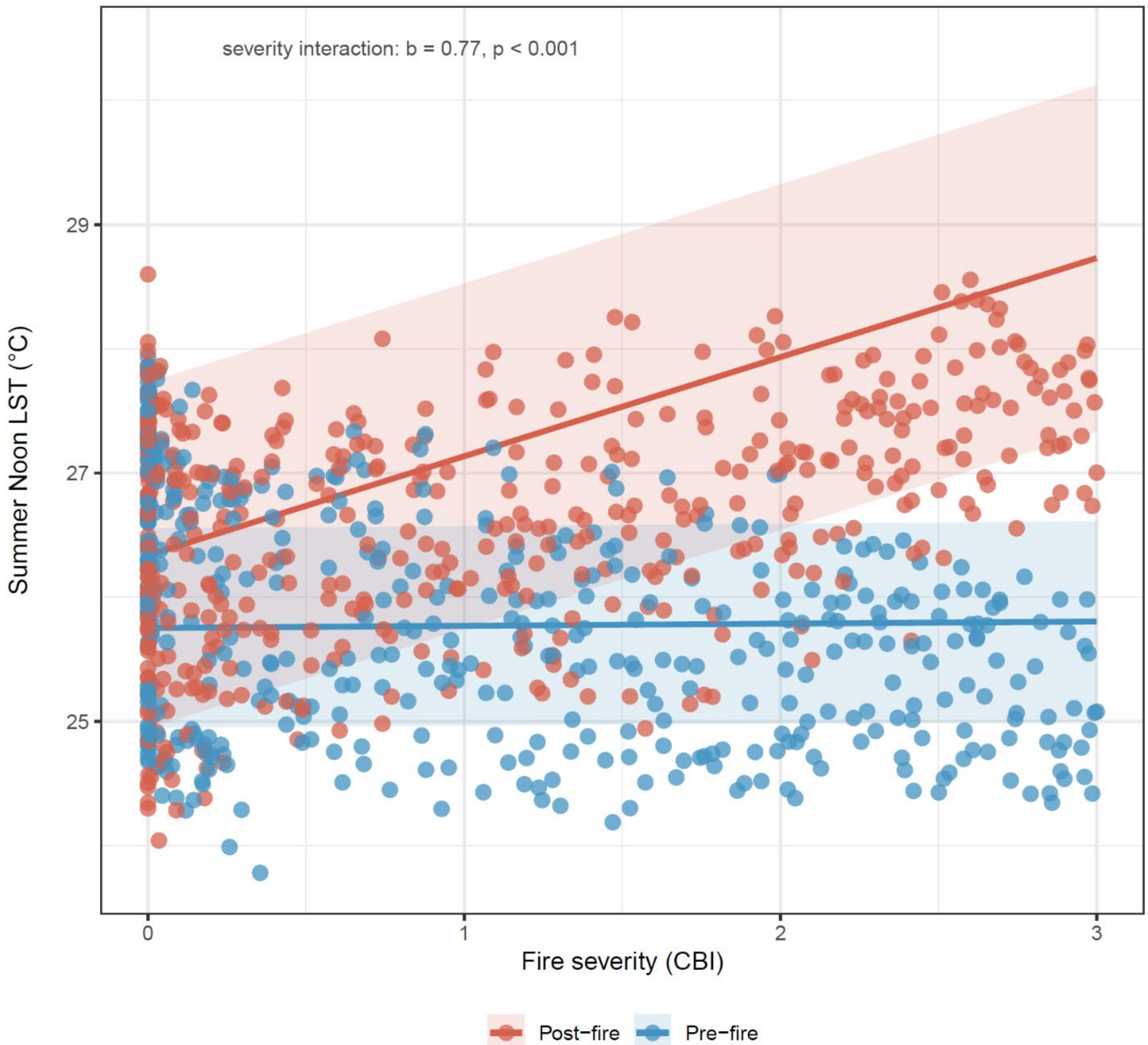

Figure 5. Burn severity altered the post-fire relationship between fire severity and summer LST. Summer noon-standardized land surface temperature is shown as a function of continuous Composite Burn Index (CBI), before and after the Lookout Fire. Predictions are from a mixed-effects model that accounts for summer climate and forest structure. Points show cell-level values and shaded bands show 95% confidence intervals. The positive post-fire relationship between CBI and summer LST, compared with the weak pre-fire relationship, indicates that higher burn severity resulted in increased summer surface warming.

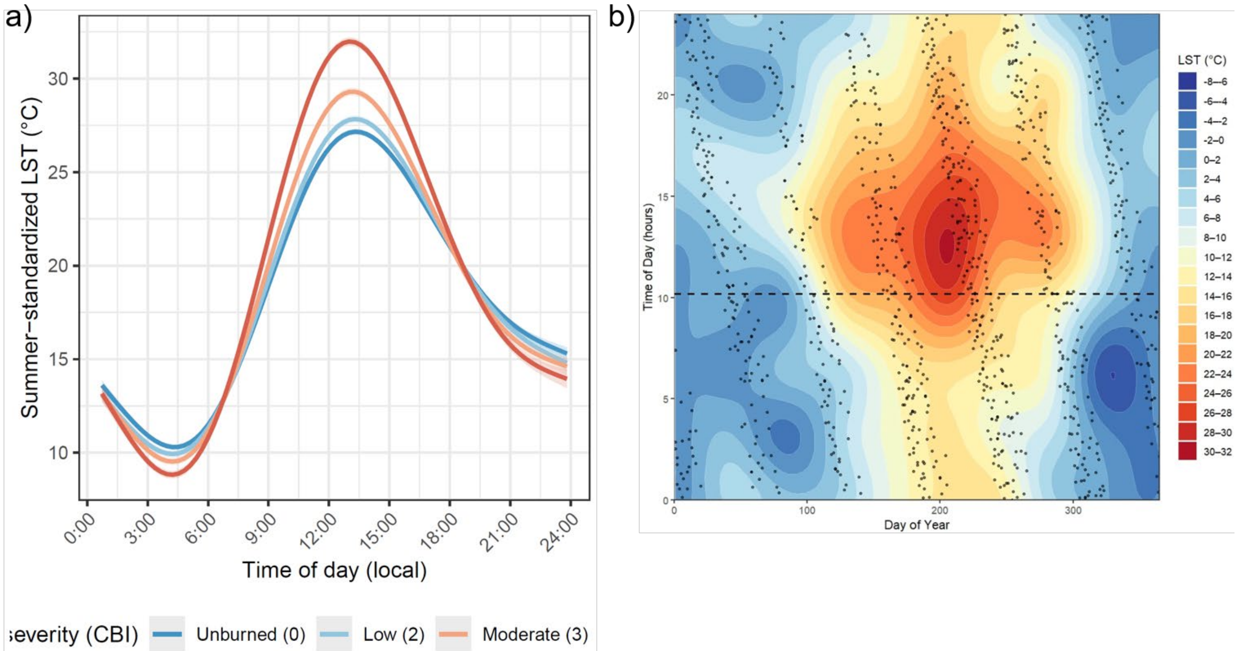

Figure 6. Diurnal structure of LST. (a) Summer-standardized diurnal LST curves for unburned, low-severity, and moderate-severity burn classes in post burn condition. Lines show fitted diurnal patterns and shaded bands show uncertainty. Burned areas were warmer during the daytime, with the largest differences near midday and early afternoon. (b) Seasonal-diurnal distribution of ECOSTRESS LST observations across day of year and time of day. The color surface shows LST contours from a GAM interaction, points show ECOSTRESS observations and their ISS-processional pattern, and the dashed horizontal line marks the typical Landsat LST acquisition overpass time which would not capture the magnitude of post-fire LST observed here.

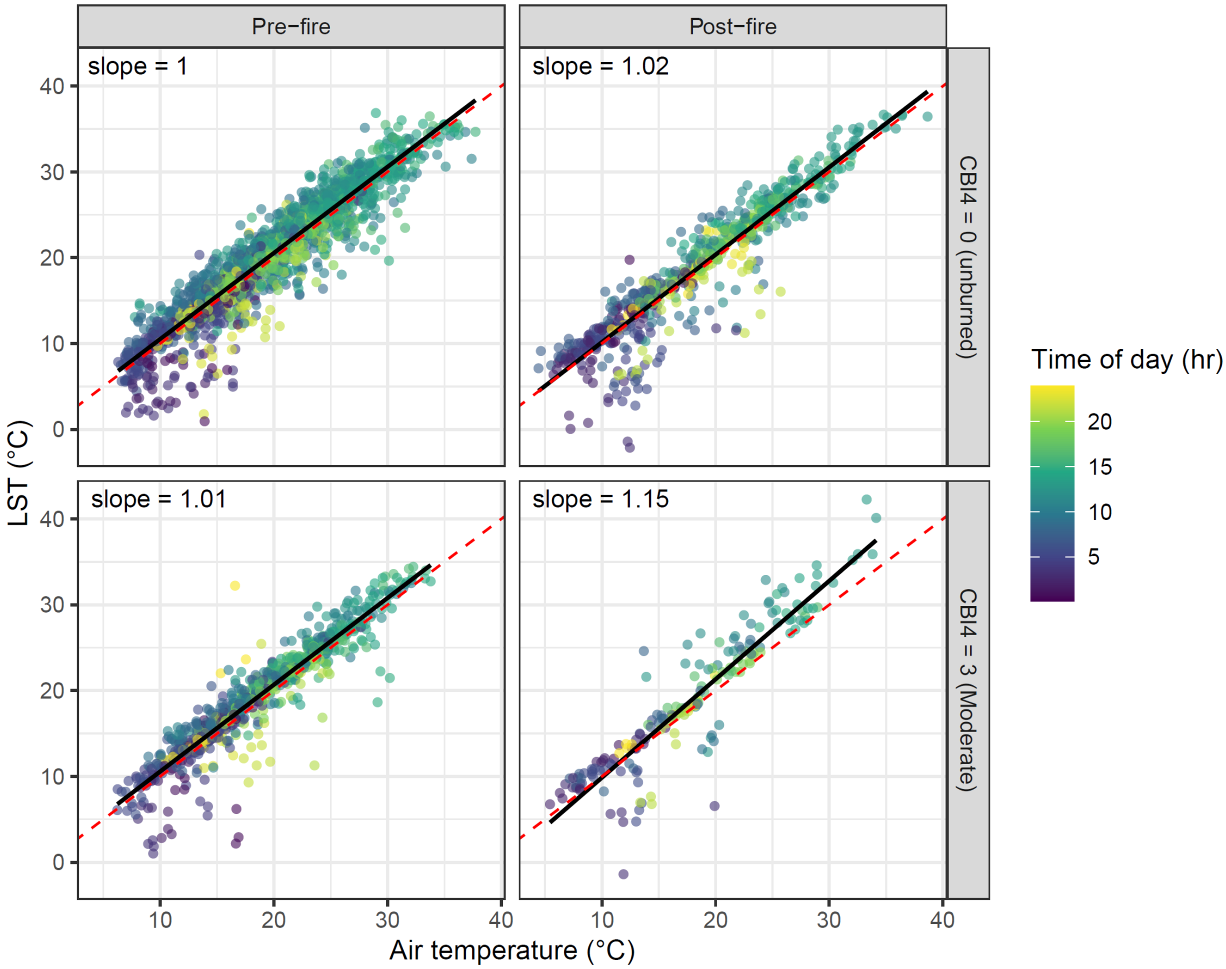

Figure 7. Fire severity modified the coupling between land surface temperature and air temperature at the Core Phenology Plots. Relationships between Summer ECOSTRESS LST observation and instantaneous air temperature are shown before and after the Lookout Fire for unburned areas and moderately burned areas. Points are colored by time of day. The red dashed lines show the 1:1 reference between LST and air temperature, and black lines show fitted relationships. Before fire, LST closely tracked air temperature across burn classes. After fire, moderately burned areas showed a steeper LST–air temperature relationship.

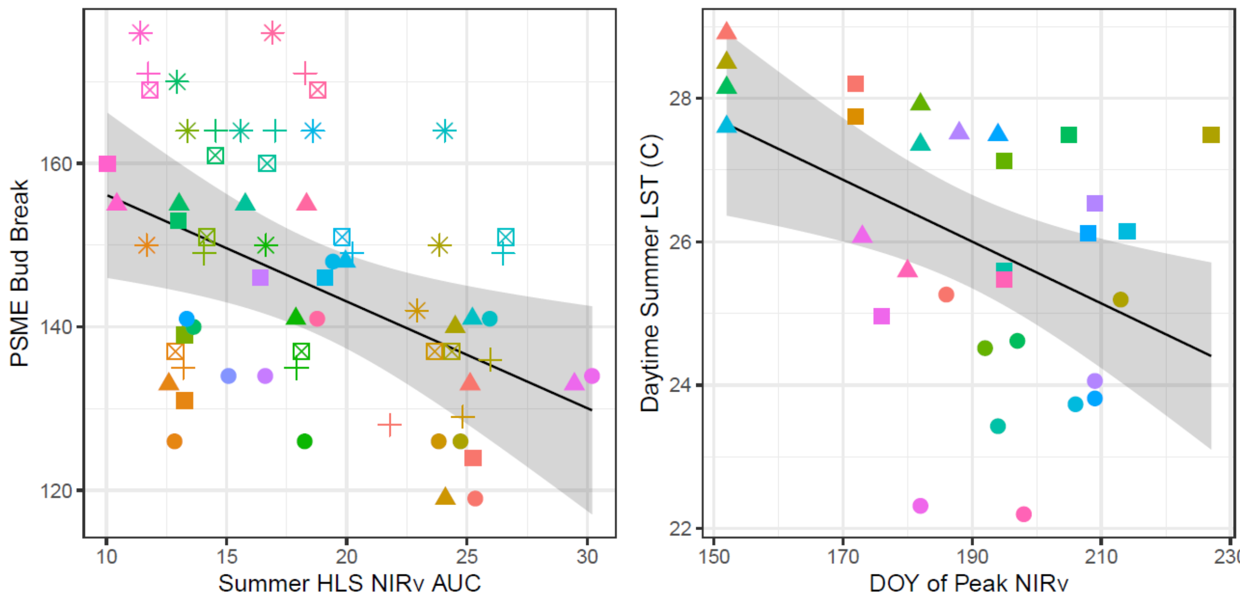

Figure 8. Links between remotely sensed vegetation phenology, field phenology, and summer surface temperature at Core Phenology Plots. (a) Relationship between summer HLS NIRv area under the curve (AUC) and field-observed Douglas-fir (Pseudotsuga menziesii; PSME) bud break. Earlier bud break was associated with greater summer NIRv accumulation. (b) Relationship between the day of year of peak NIRv and noon summer ECOSTRESS LST. Earlier peak NIRv was associated with warmer summer surface temperatures. Points represent plot-year means, black lines show fitted relationships, and gray bands show 95% confidence intervals. These relationships link field phenology, satellite vegetation indices, and remotely sensed surface temperature, providing a basis for interpreting post-fire phenological shifts in relation to surface microclimate.

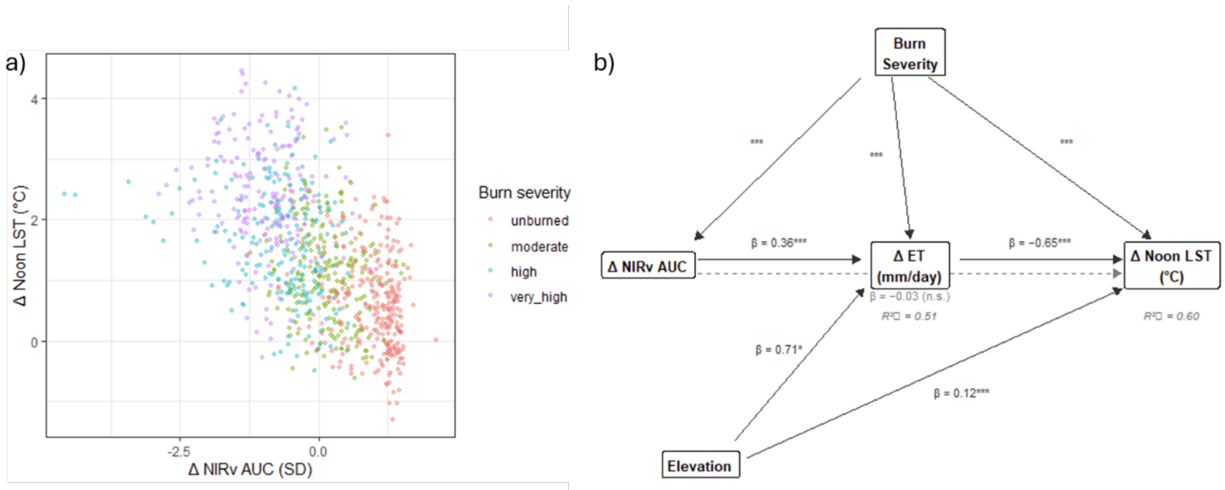

Figure 9. Coupled post-fire changes in vegetation phenology, evapotranspiration, and surface temperature across burn-severity classes. (a) Relationship between post-fire change in seasonal NIRv area under the curve (Δ NIRv AUC, standardized units) and change in noon-corrected land surface temperature (Δ Noon LST, °C), colored by burn-severity class. Greater reductions in NIRv AUC were generally associated with larger increases in noon LST, especially in high- and very-high-severity plots. (b) Structural equation model linking burn severity, elevation, Δ NIRv AUC, Δ evapotranspiration (ET), and Δ Noon LST in a test of mediation framework. Solid arrows indicate significant pathways and dashed arrows indicate non-significant pathways; standardized path coefficients are shown next to arrows. Burn severity affected vegetation phenology, ET, and noon LST, while reductions in NIRv AUC were associated with lower ET, and lower ET was associated with higher noon LST but after including ET as a mediator there is no direct effect of NIRv on LST (Δ).

Supplementary Information

Title: Wildfire severity reshapes remotely sensed surface temperature and vegetation phenology in a Western Cascades forest ecosystem

Daniel M. Griffith[1]*
Christopher J. Still[2]
Matthew G. Betts[2]
Amelia Fitch[2]
Hannah R. Sachs[2]
Mark D Schulze[2]

[1] Department of Ecology and Evolution, Stony Brook University, Stony Brook, NY, USA. 11790
[2] Forest Ecosystems and Society, Oregon State University, Corvallis, OR, 97331

Contents

Supplementary Tables

Supplementary Figures

Figure S7. Seasonal variation in modeled diurnal LST cycles from harmonic regression.

Figure S8. Standardized seasonal ECOSTRESS LST observations after harmonic correction.

Figure S9. Seasonal LST time series by burn-severity class.

Figure S10. Distribution of land surface temperature departures from air temperature.

Figure S11. HLS NIRv time series for all TV075 core phenology plots.

Figure S12. Summary of HLS NIRv comparisons with TV075 field phenology.

Figure S13. Douglas-fir budbreak timing across site-year NIRv curves.

Figure S14. Species-specific phenology alignment with NIRv at three contrasting sites.

Figure S15. Community- and species-level phenology stages plotted against the HJA-wide seasonal NIRv curve.

Table S1. Harmonic regression model selection for ECOSTRESS LST standardization. Model selection results for candidate harmonic regression models used to standardize ECOSTRESS LST by day of year and time of day. Models were compared using maximum likelihood. Marginal R^2 (R^2m) represents variance explained by fixed effects, and conditional R^2 (R^2c) represents variance explained by fixed and random effects. The selected model included seasonal harmonics, diurnal harmonics, their interaction, and a site-specific diurnal random slope, and was refit with REML for final parameter estimation and prediction.

Model	n parameters	R^2m	R^2c	LRT p	Interpretation
Fourier seasonal + diurnal model	13	0.734	0.742	—	Baseline harmonic model with seasonal and diurnal cycles.
Seasonal × diurnal interaction model	37	0.762	0.769	<0.001	Improved fit by allowing diurnal LST structure to vary across the year.
Site-specific diurnal model	39	0.766	0.774	<0.001	Final model; added site-specific diurnal variation and provided the best-supported standardization model.

Table S2. Landscape-scale pre- and post-fires mixed model selection for post-fire LST analyses. Model selection results for landscape-scale mixed-effects BACI models of ECOSTRESS land surface temperature. Models were compared using maximum likelihood. Delta AIC is calculated relative to the lowest-AIC model in this set.

Model	n parameters	AIC	ΔAIC	BIC	logLik	LRT p	Interpretation
Null model	4	722818	40458	722857	−361405	—	Random effects only.
Climate-only model	10	721397	39037	721494	−360688	<0.001	Climate covariates strongly improved fit.
Climate + fire-phase model	11	688322	5962	688428	−344150	<0.001	Adding fire phase greatly improved fit.
Add canopy height	12	687475	5115	687591	−343726	<0.001	Canopy structure improved model fit.
Add elevation	13	687498	5138	687624	−343736	1.000	Elevation did not improve this intermediate model.
Add burn-severity structure	14	687451	5091	687587	−343712	<0.001	Burn-severity structure improved model fit.
Full BACI model	16	687453	5093	687609	−343711	0.445	Added terms did not improve fit relative to the simpler model.
BACI model with additional fire interactions	29	682360	0	682641	−341151	<0.001	Best-supported landscape model; additional fire-climate interactions substantially improved fit.

Table S3. Core phenology plot LST-air-temperature BACI model selection. Model selection results for mixed-effects BACI models evaluating ECOSTRESS LST-air temperature coupling at the core phenology plots. Models were compared using maximum likelihood. Delta AIC is calculated relative to the lowest-AIC model in this set.

Model	n parameters	AIC	ΔAIC	BIC	logLik	LRT p	Interpretation
Null model	4	24360	7695	24384	−12175.7	—	Random effects only.
Air-temperature model	5	16871	206	16902	−8430.7	<0.001	Instantaneous air temperature explained most LST variation.
Air temperature × fire phase × CBI4	11	16855	190	16924	−8416.6	<0.001	Fire phase and burn severity improved the air-temperature model.
Selected BACI model	24	16665	0	16814	−8308.6	<0.001	Best-supported model balancing air temperature, fire phase, CBI4, climate, and structure covariates.
Full interaction model	32	16676	11	16875	−8306.1	0.769	Additional interaction terms did not improve model fit enough to justify added complexity.

Table S4. Model selection table for change model. Model selection results for mixed-effects BACI models evaluating ECOSTRESS LST-air temperature coupling … Table S5 contains the model parameters.

Model	n parameters	AIC	ΔAIC	BIC	logLik	LRT p	Interpretation
Base: NIRv × severity + elevation	11	2194.0	357.0	2246.0	-1086.0	—	Reference model
+ climate deltas	15	1936.0	99.3	2008.0	-953.0	<0.001	Do year-to-year climate anomalies explain warming?
+ climate levels	15	1969.0	132.0	2041.0	-969.0	<0.001	Do absolute climate conditions explain warming?
Full: all climate + canopy, no interaction	18	1853.0	15.9	1939.0	-908.0	<0.001	Full climate-control model; reference for interaction models
NIRv × climate, full	20	1843.0	6.5	1939.0	-902.0	<0.001	Is the NIRv–LST relationship modulated by climate?
NIRv × climate, pruned	19	1837.0	0.0	1928.0	-899.0	0.432	Best-supported model; unsupported interactions removed

Table S5. Linear mixed-effects model predicting post-fire change in corrected noon land surface temperature. Response variable was Δ predicted noon LST. The model included a random intercept for grid cell. Number of observations = 888; number of cells = 444. Random-intercept variance = 0.095; residual variance = 0.332. Models were fit by REML, and p-values were calculated using Satterthwaite's method. Burn-severity effects are relative to the unburned reference class.

Predictor	**Estimate**	**SE**	**df**	**t**	**p**
Intercept	0.92	0.065	483.75	14.2	<0.001
Δ NIRv AUC	-0.171	0.043	531.05	-3.98	<0.001
Tmax	-0.897	0.136	446.68	-6.62	<0.001
30-day precipitation	-2.27	0.432	435.48	-5.26	<0.001
Vapor pressure	-0.546	0.154	441.5	-3.55	<0.001
Solar radiation	-0.158	0.041	458.94	-3.83	<0.001
Moderate burn severity	0.245	0.08	459.55	3.06	0.002
High burn severity	0.443	0.1	481.06	4.44	<0.001
Very high burn severity	1.063	0.109	491.85	9.76	<0.001
Elevation	-0.129	0.066	427.42	-1.95	0.052
Percent open vegetation	0.154	0.028	430.59	5.46	<0.001
Δ Tmax	0.227	0.056	792.34	4.04	<0.001
Δ 30-day precipitation	2.302	0.408	436.37	5.64	<0.001
Δ solar radiation	0.188	0.032	820.72	5.96	<0.001
Δ vapor pressure	0.725	0.151	452.56	4.8	<0.001
Δ NIRv AUC × Tmax	0.143	0.032	553.94	4.43	<0.001
Δ NIRv AUC × 30-day precipitation	0.102	0.025	524.88	4.12	<0.001

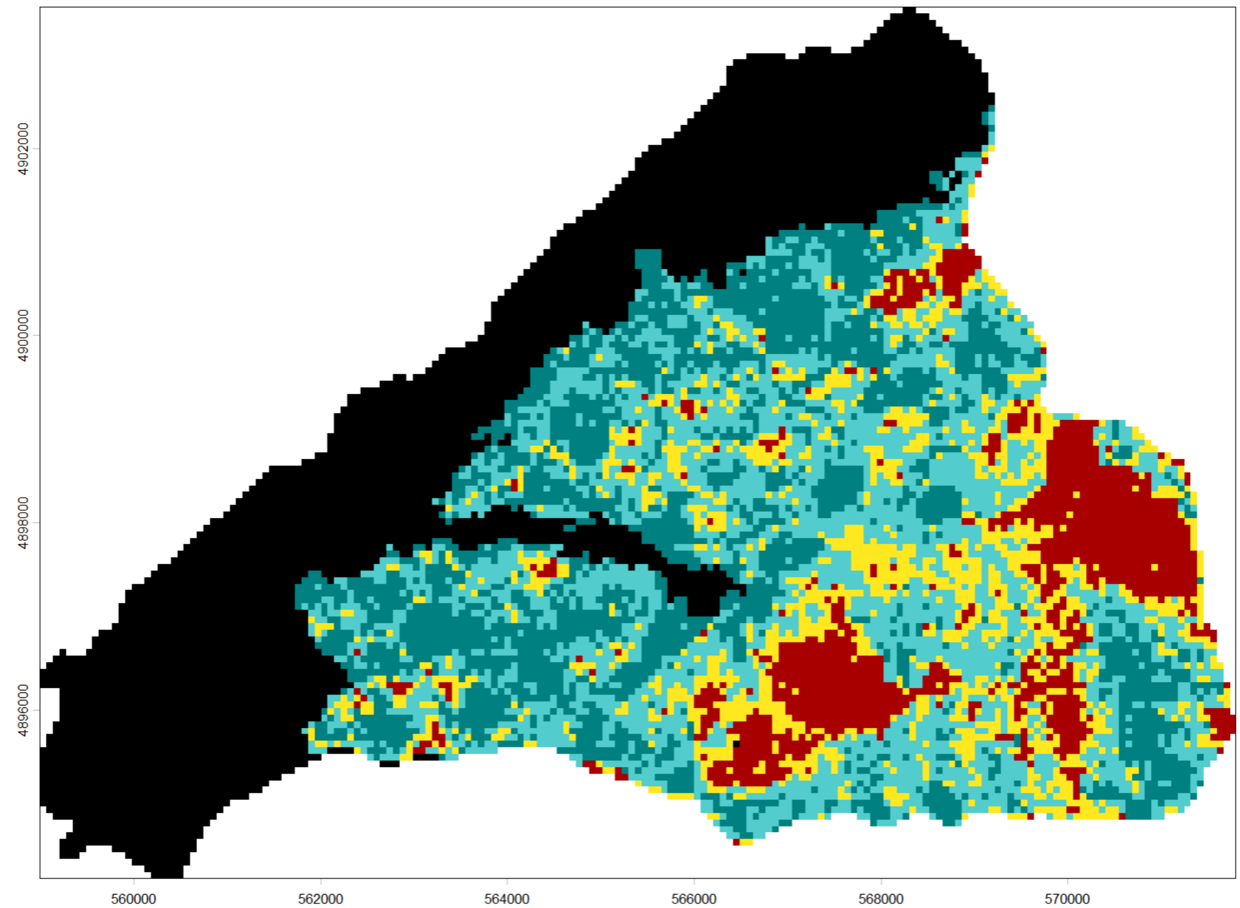

Figure S1. RAVG burn-severity classification for the H.J. Andrews Experimental Forest following the 2023 Lookout Fire. Spatial distribution of RAVG CBI4 burn-severity classes within the H.J. Andrews Experimental Forest and Lookout Fire perimeter. Unburned or unchanged areas are shown in black, with increasing burn severity shown by progressively warmer colors. This classification was used to define burn-severity groups for ECOSTRESS LST anomaly analyses, BACI contrasts, and the spatial sampling design.

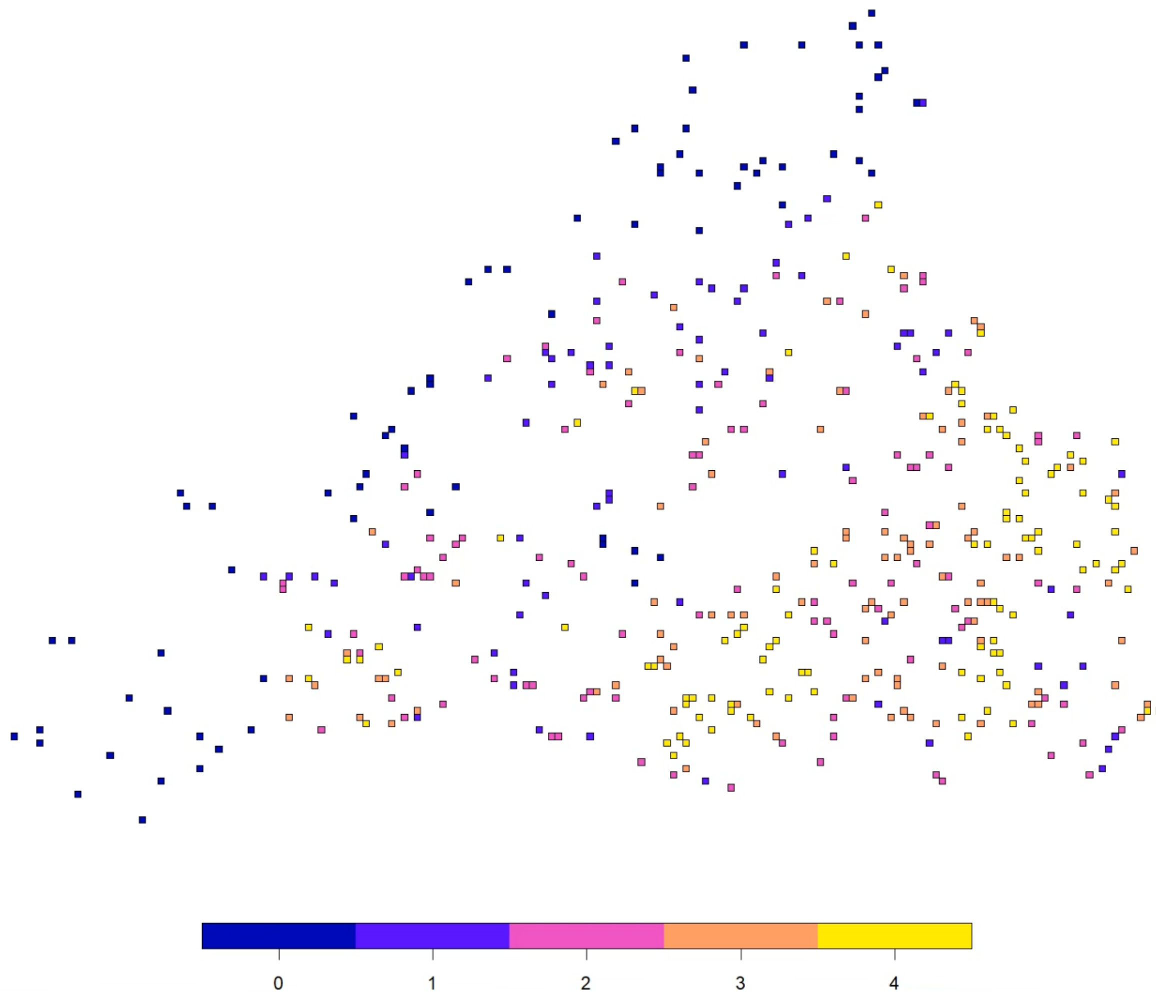

Figure S2. Spatial distribution of ECOSTRESS sampling cells across burn-severity classes. Map of sampled ECOSTRESS cells used in the landscape-scale LST analyses, colored by RAVG CBI4 burn-severity class. Sampling points span unburned/unchanged, low-, moderate-, and high-severity areas across the HJA landscape, providing spatial replication across the topographic and fire-severity gradients used in the BACI and seasonal anomaly analyses.

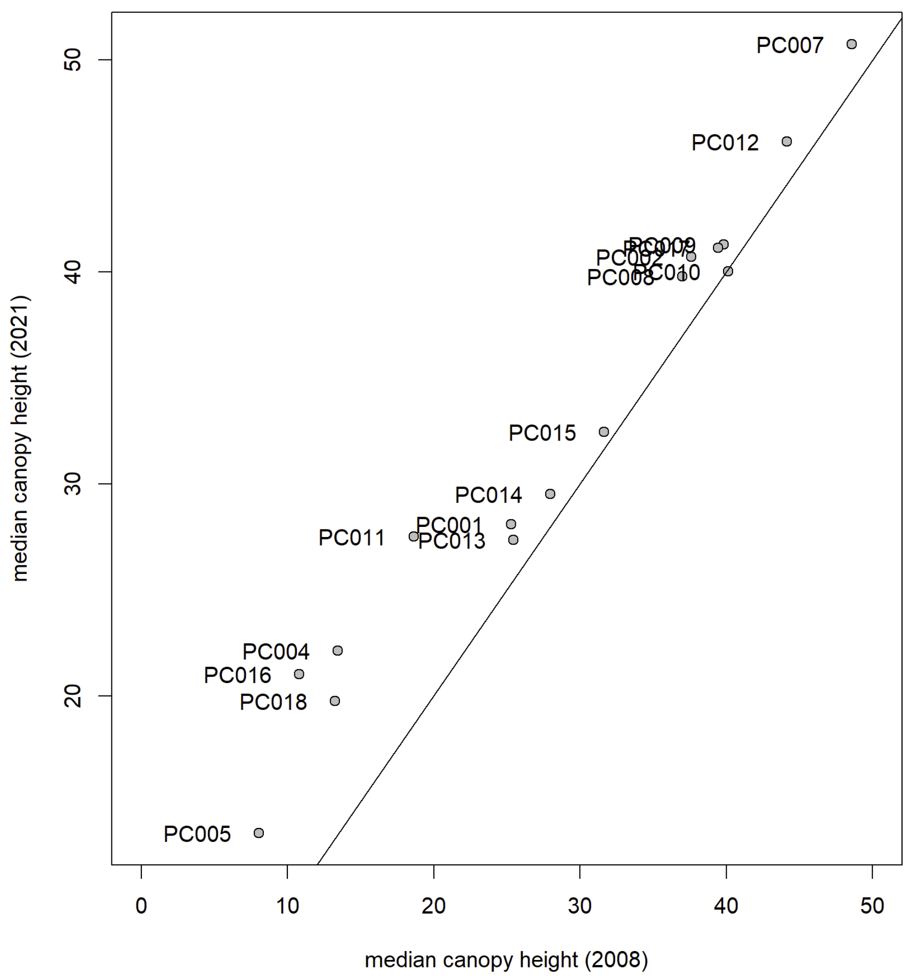

Figure S3. Change in canopy height at core phenology plots between 2008 and 2021. Median canopy height from airborne LiDAR-derived canopy height products in 2008 and 2021 for core phenology plots. The 1:1 line indicates no change between years. Most plots fall above the line, indicating increases in canopy height over this period, while variation among plots reflects differences in stand structure, successional state, and disturbance history prior to the Lookout Fire.

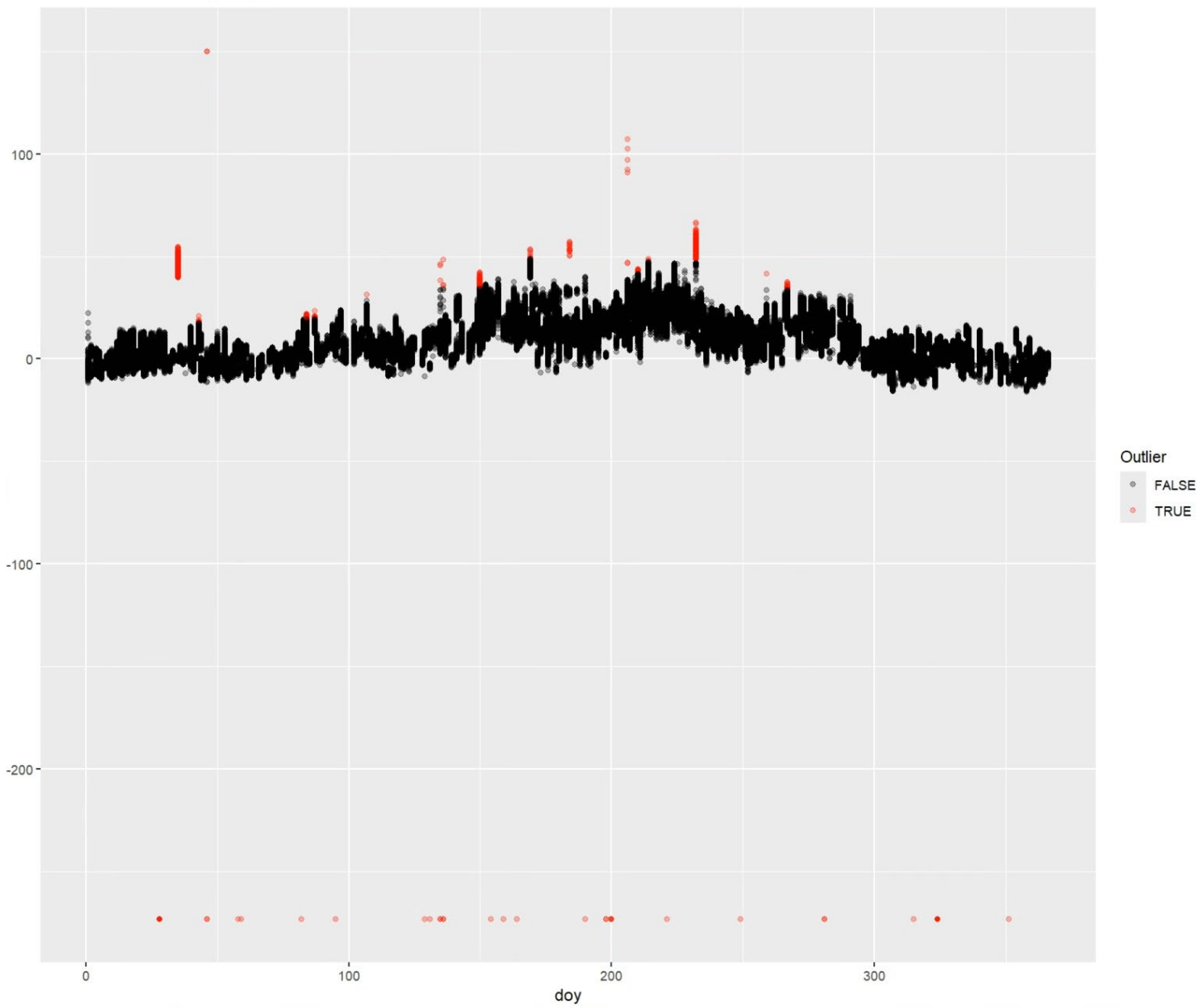

Figure S4. ECOSTRESS land surface temperature outlier screening. Initial ECOSTRESS LST observations plotted by day of year, with outliers identified using a seasonal interquartile range filter: values below Q1 − 2.5 × IQR or above Q3 + 2.5 × IQR were flagged as outliers. Flagged values included unrealistically low LST values and isolated extreme high values. These observations were removed before seasonal, diurnal, and analyses

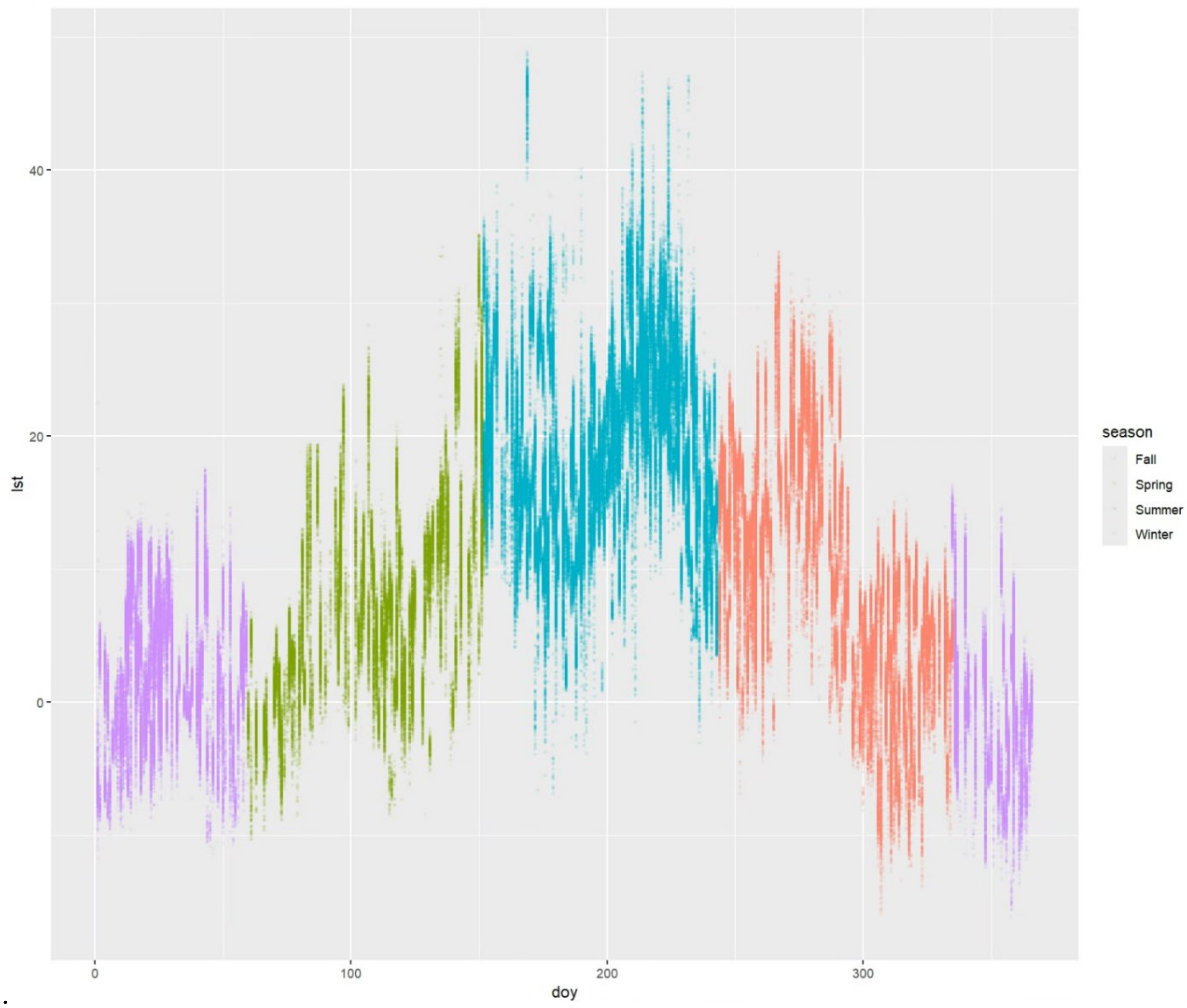

.

Figure S5. Seasonal distribution of ECOSTRESS LST observations after outlier removal. Cleaned ECOSTRESS LST observations plotted by day of year and colored by season. The filtered data retain the expected seasonal temperature structure, with lowest LST values during winter, increasing temperatures during spring, highest values during summer, and declining temperatures during fall. This figure verifies that outlier removal preserved the seasonal thermal signal used in subsequent analyses.

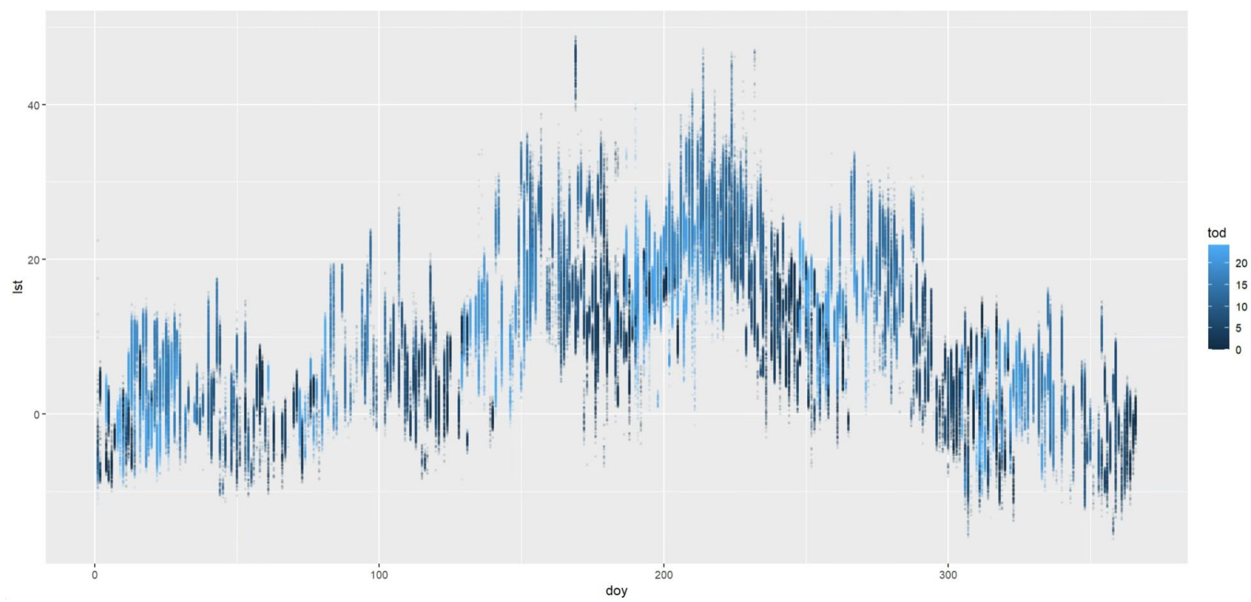

Figure S6. ECOSTRESS time-of-day sampling across the seasonal cycle. ECOSTRESS LST observations plotted by day of year and colored by time of day. The distribution of observations shows that the ISS orbit samples the landscape at varying local times rather than a fixed overpass time. This time-of-day variation creates the potential for aliasing seasonal and diurnal LST patterns, motivating the harmonic standardization of LST by both day of year and time of day.

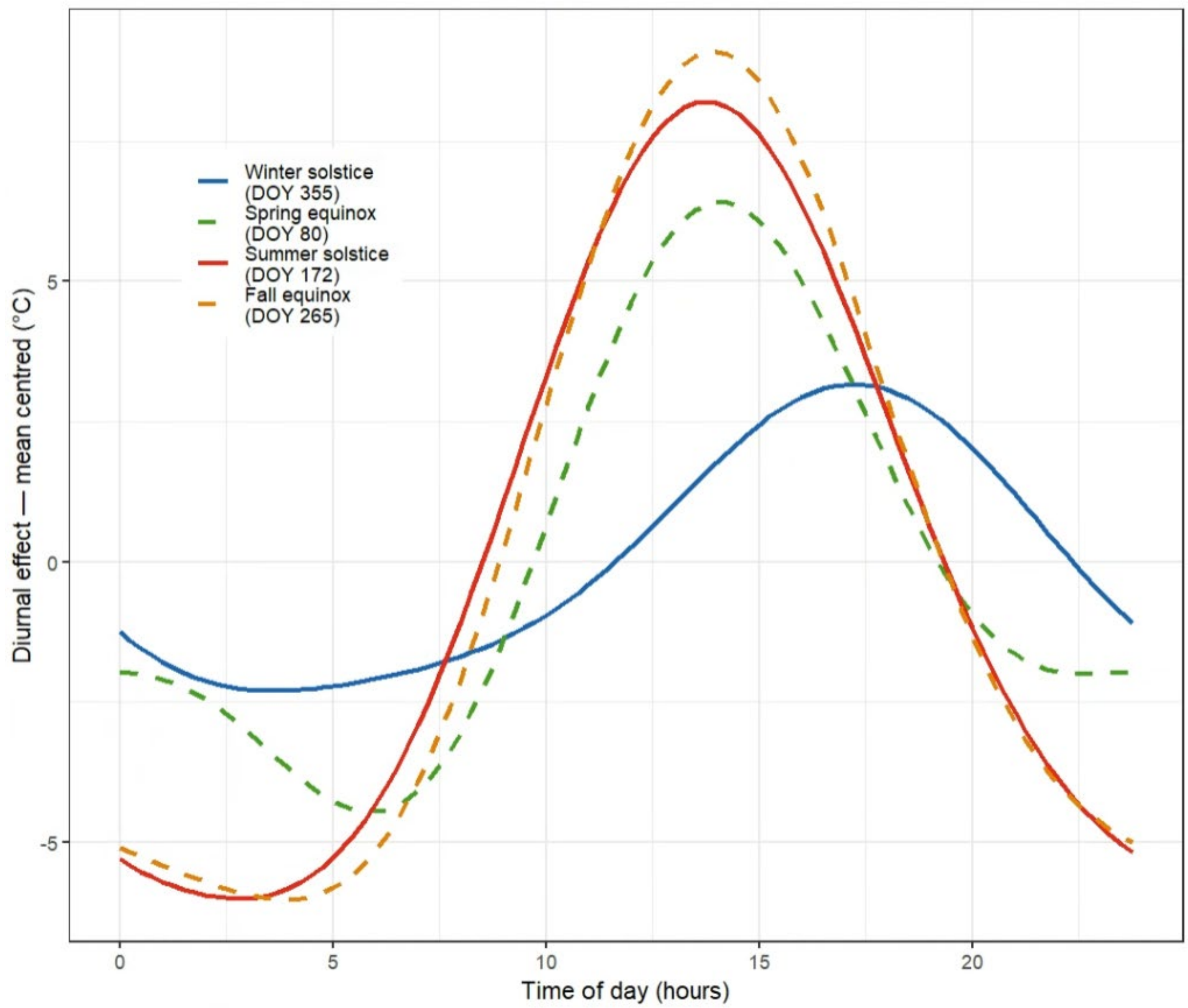

Figure S7. Seasonal variation in modeled diurnal LST cycles from harmonic regression. Predicted diurnal LST effects from the harmonic regression model at the winter solstice, spring equinox, summer solstice, and fall equinox. Diurnal amplitude was greatest during summer and fall and weakest during winter, demonstrating why ECOSTRESS LST required time-of-day standardization before comparing pre- and post-fire observations.

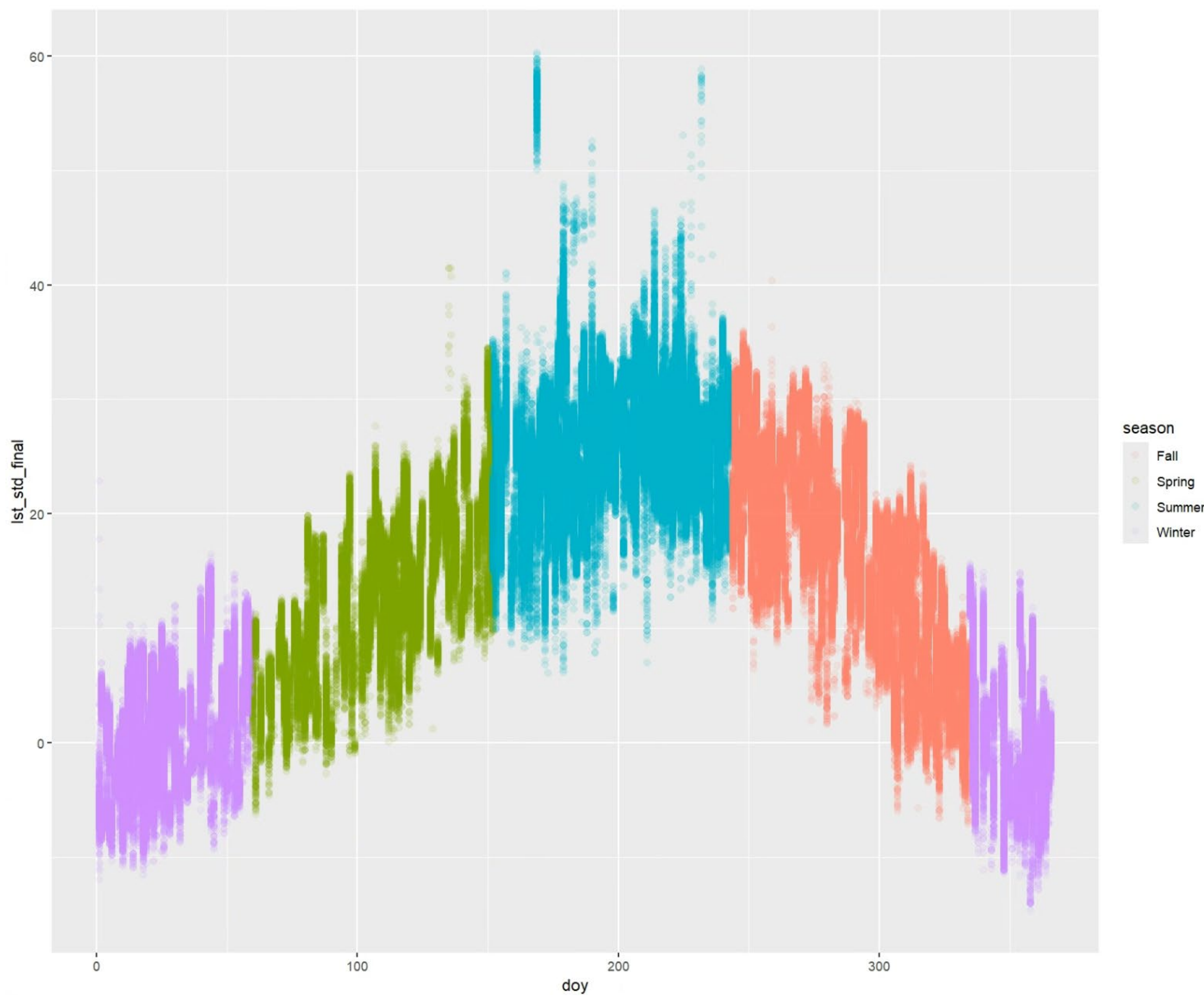

Figure S8. Standardized seasonal ECOSTRESS LST observations after harmonic correction. Cleaned and standardized ECOSTRESS LST observations plotted by day of year and colored by season. Compared with the unstandardized observations, this distribution shows the retained seasonal structure after outlier screening and standardization, providing a diagnostic check for the LST data used in the main seasonal anomaly and statistical analyses.

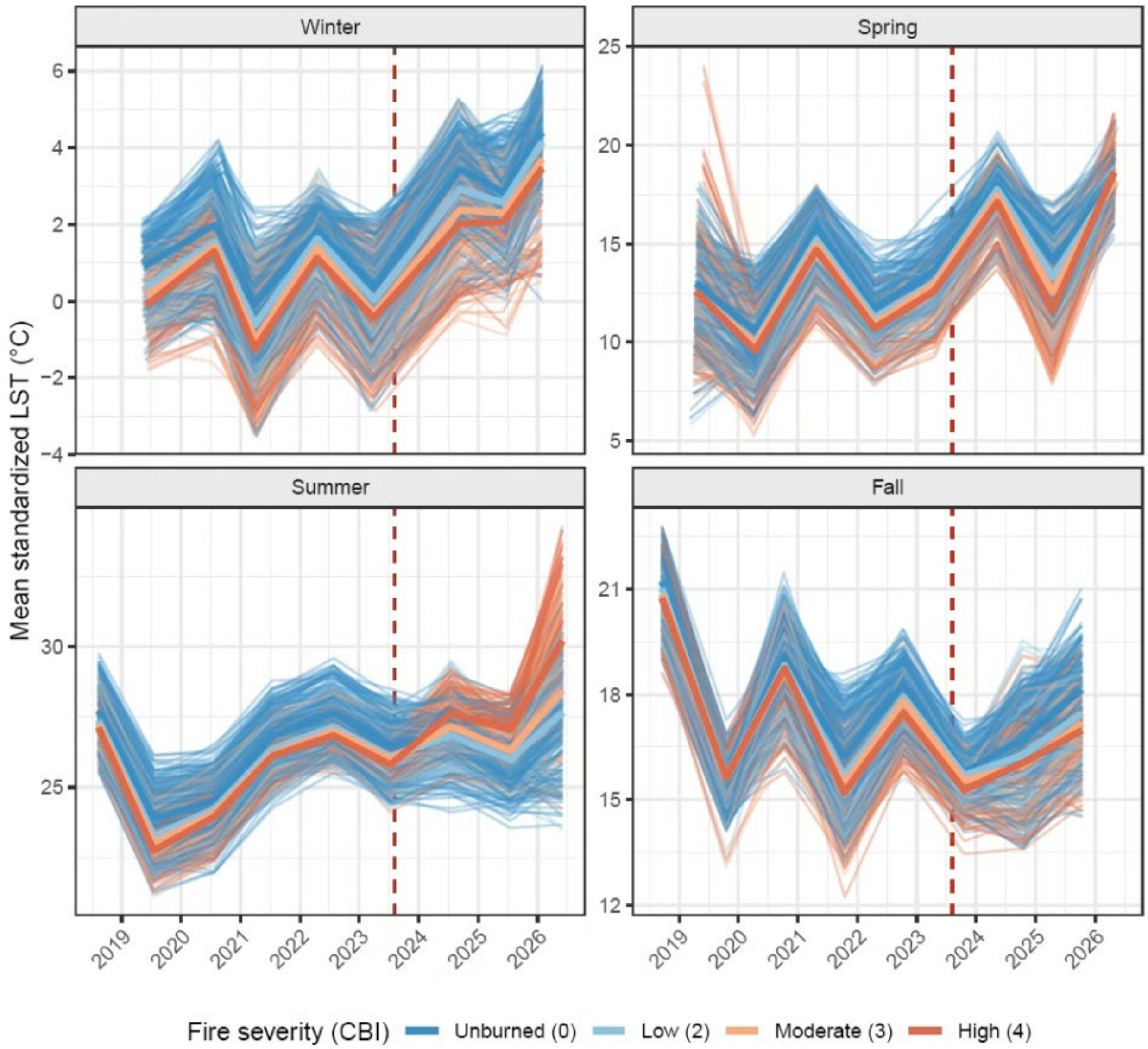

Figure S9. Seasonal LST time series by burn-severity class. Mean standardized LST time series for winter, spring, summer, and fall, grouped by RAVG CBI4 burn-severity class. Thin lines show cell-level trajectories and thick lines show class-level trends. The dashed vertical line marks the 2023 Lookout Fire. This figure complements the main-text anomaly analysis by showing the underlying standardized seasonal time series, with the strongest post-fire divergence occurring during summer in higher-severity burn classes.

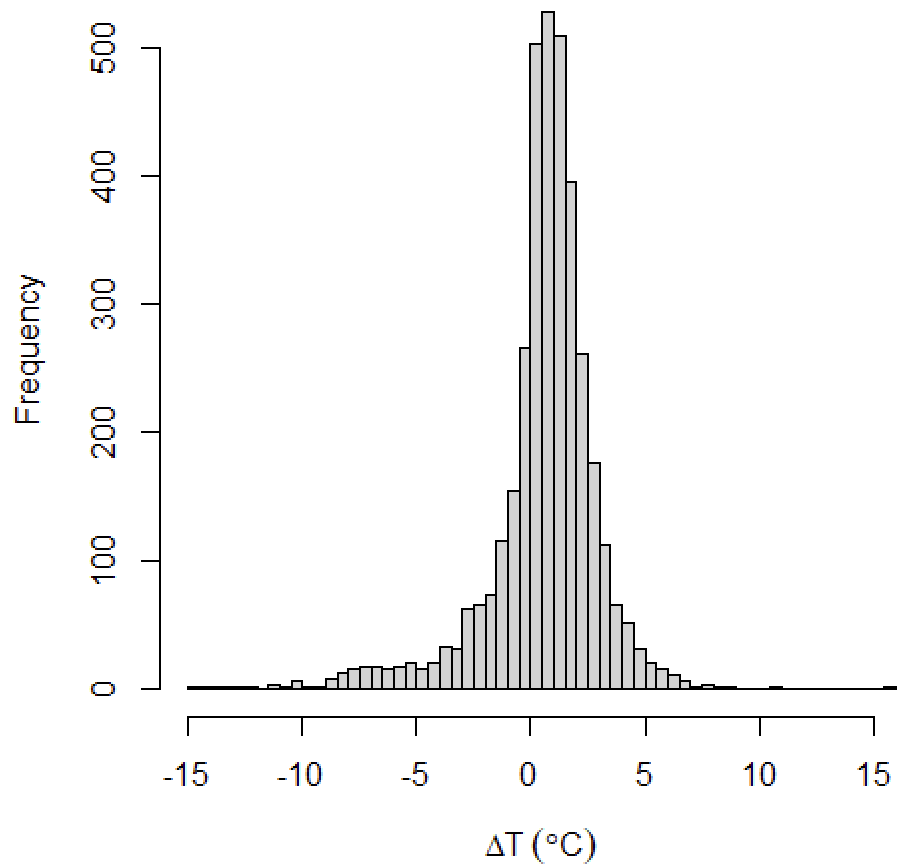

Figure S10. Distribution of land surface temperature departures from air temperature. Histogram of ΔT, calculated as ECOSTRESS LST minus instantaneous air temperature, across core phenology plot observations. Values are centered above 0 °C, indicating that ECOSTRESS LST was generally warmer than air temperature. This supports the main-text analysis of LST–air temperature coupling and provides context for interpreting post-fire changes in surface heating.

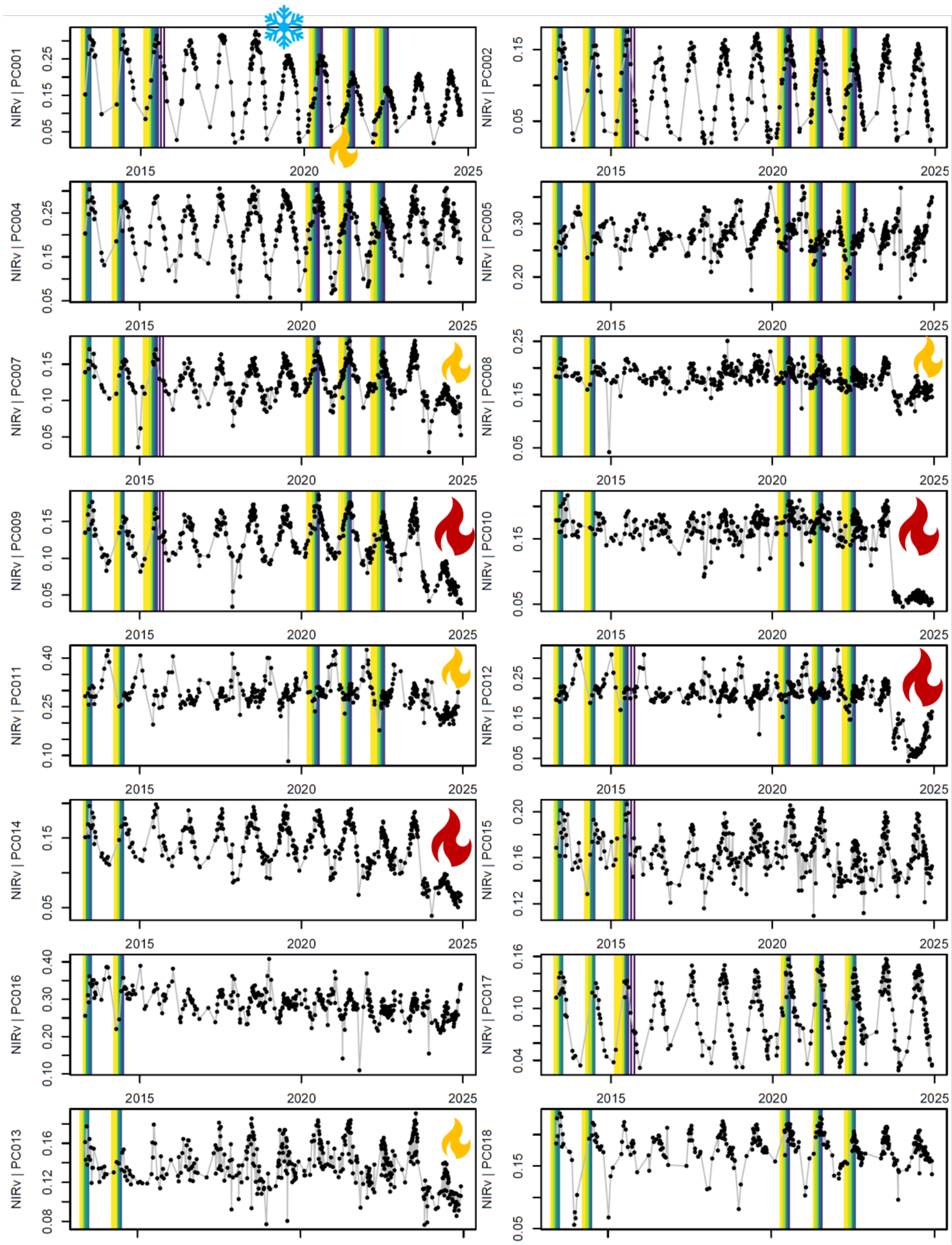

Figure S11. HLS NIRv time series for all TV075 core phenology plots. Near-infrared reflectance of vegetation (NIRv) time series from Harmonized Landsat–Sentinel-2 observations for all core phenology plots in the TV075 dataset. Points show cloud- and quality-screened observations. Colored vertical bands indicate field-observed phenological stages, with earlier phenophases shown in yellow shades and later phenophases shown in green/blue/purple shades. The snowflake indicates the 2019 snowdown and the flame symbols highlight the Lookout fire impacts. The plot-level time series shows strong seasonal and interannual variation in NIRv, as well as marked declines at plots affected by recent wildfire.

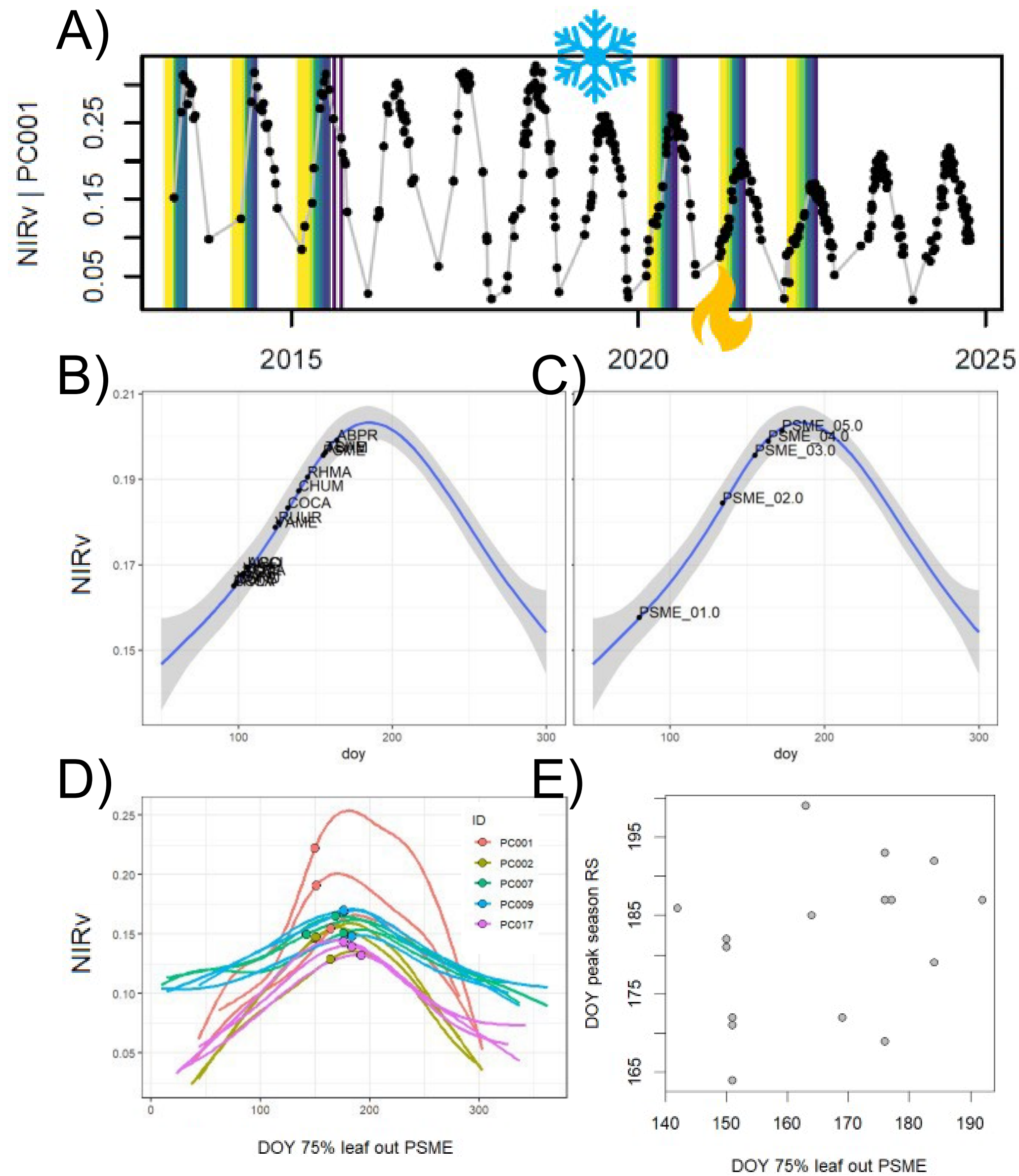

Figure S12. Summary of HLS NIRv comparisons with TV075 field phenology. Multi-panel summary of relationships between HLS NIRv and field-observed phenology from TV075. (a) Example NIRv time series for PC001, with vertical colored bands indicating field phenophase dates and symbols marking major disturbance events. (b) Median budbreak day of year for species tracked in TV075 plotted along the mean seasonal NIRv curve, showing that species-level phenology spans the green-up period. (c) Douglas-fir phenological stages plotted along the same NIRv curve; PSME_03 indicates budbreak and PSME_05 indicates 75% leaf out. (d) Site-year NIRv curves with in situ 75% leaf-out dates, showing that phenological stages occur at consistent positions within sites but vary among sites. (e) Example comparison showing that simple remote-sensing phenology dates do not always correspond directly to field-observed phenophase timing.range from earlier (PC001) to later (PC017). E) Phenological stages from Remote Sensing do not associate with ground measurements, for example 75% leaf out.

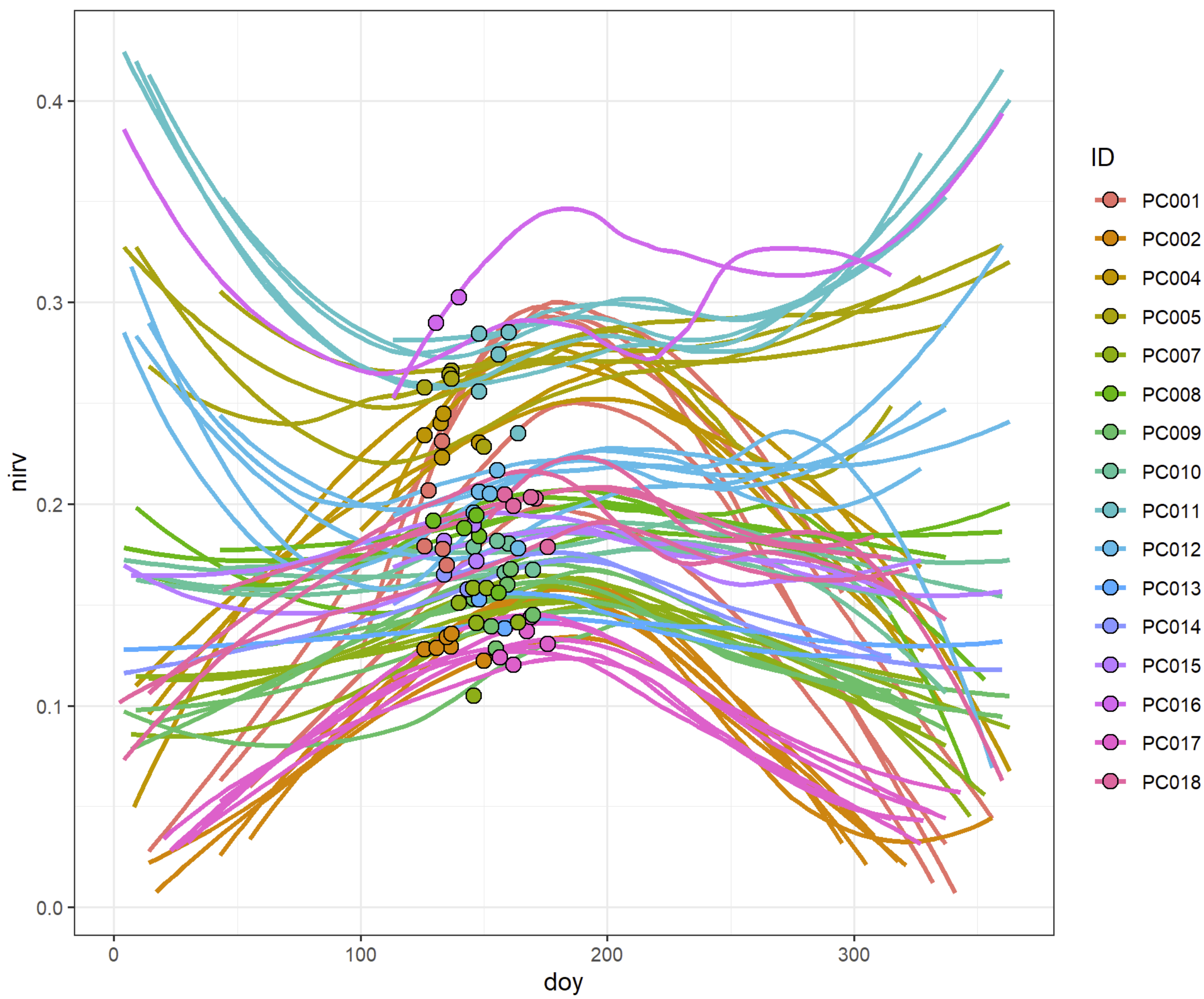

Figure S13. Douglas-fir budbreak timing across site-year NIRv curves. Site-year HLS NIRv curves for core phenology plots with field-observed Douglas-fir budbreak dates overlaid as points. Curves are colored by plot. Budbreak generally occurs during the rising portion of the NIRv seasonal curve, but its position varies among plots and years, indicating that plot-specific canopy composition, disturbance history, and site conditions influence the relationship between field-observed phenology and remotely sensed greenness. Some site-year curves also show a mid-season ‘smile’ pattern consistent with sun-angle effects on the HLS time series.

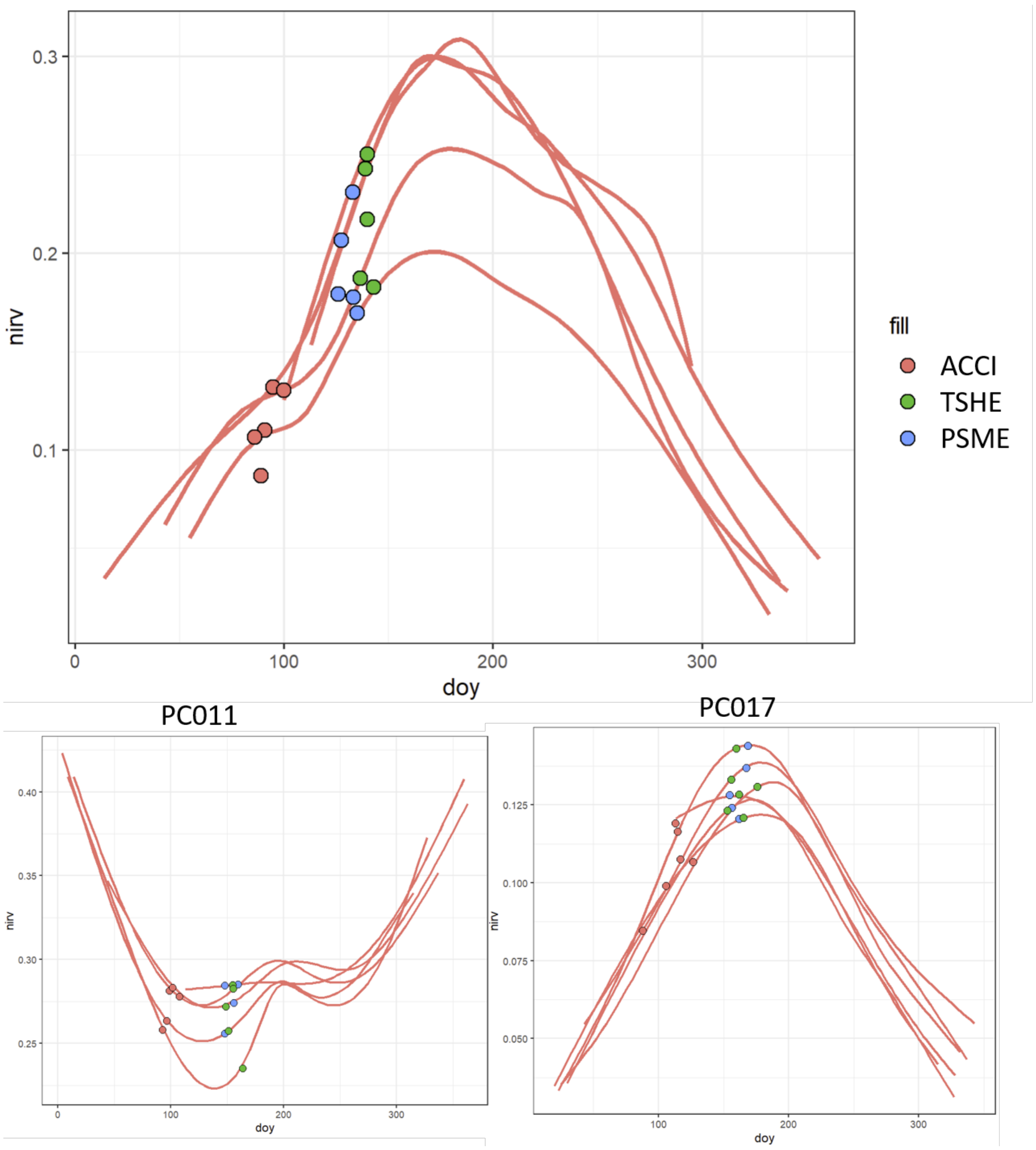

Figure S14. Species-specific phenology alignment with NIRv at three contrasting sites. Examples of field-observed phenological stages for three focal species plotted on site-level HLS NIRv curves at three core phenology plots. The examples show that species can align with NIRv seasonality in different ways depending on site context. This supports the interpretation that NIRv captures integrated canopy and understory phenological activity rather than a one-to-one signal from any single species.

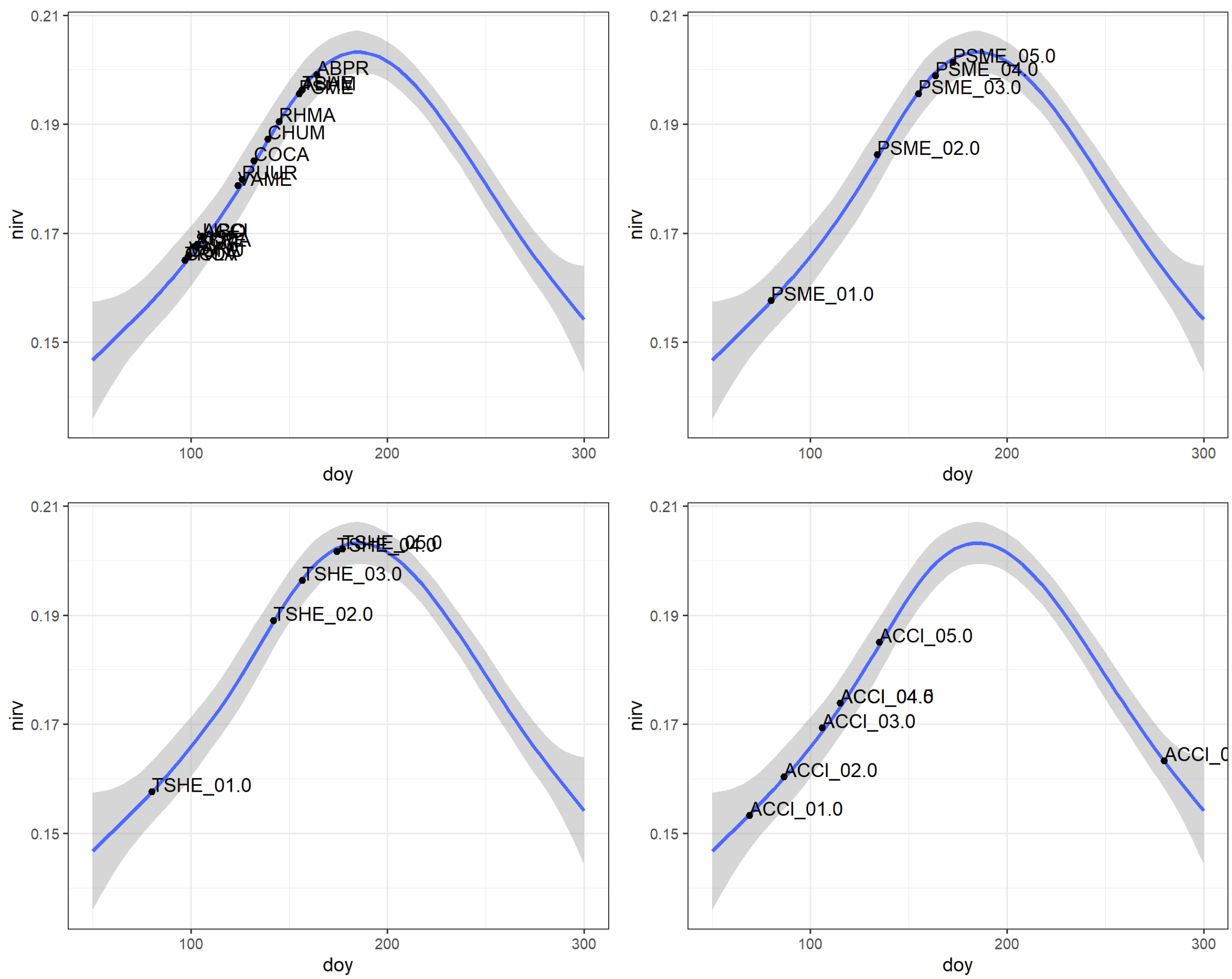

Figure S15. Community- and species-level phenology stages plotted against the HJA-wide seasonal NIRv curve. Phenological stage timing for the broader TV075 plant community and three focal species plotted on the mean HJA-wide seasonal NIRv curve. The panels show how field phenology codes align with day of year and the broader seasonal trajectory of remotely sensed greenness. Early phenophases occur on the rising portion of the NIRv curve, while later leaf expansion and senescence stages occur near the peak and declining portions of the seasonal trajectory.

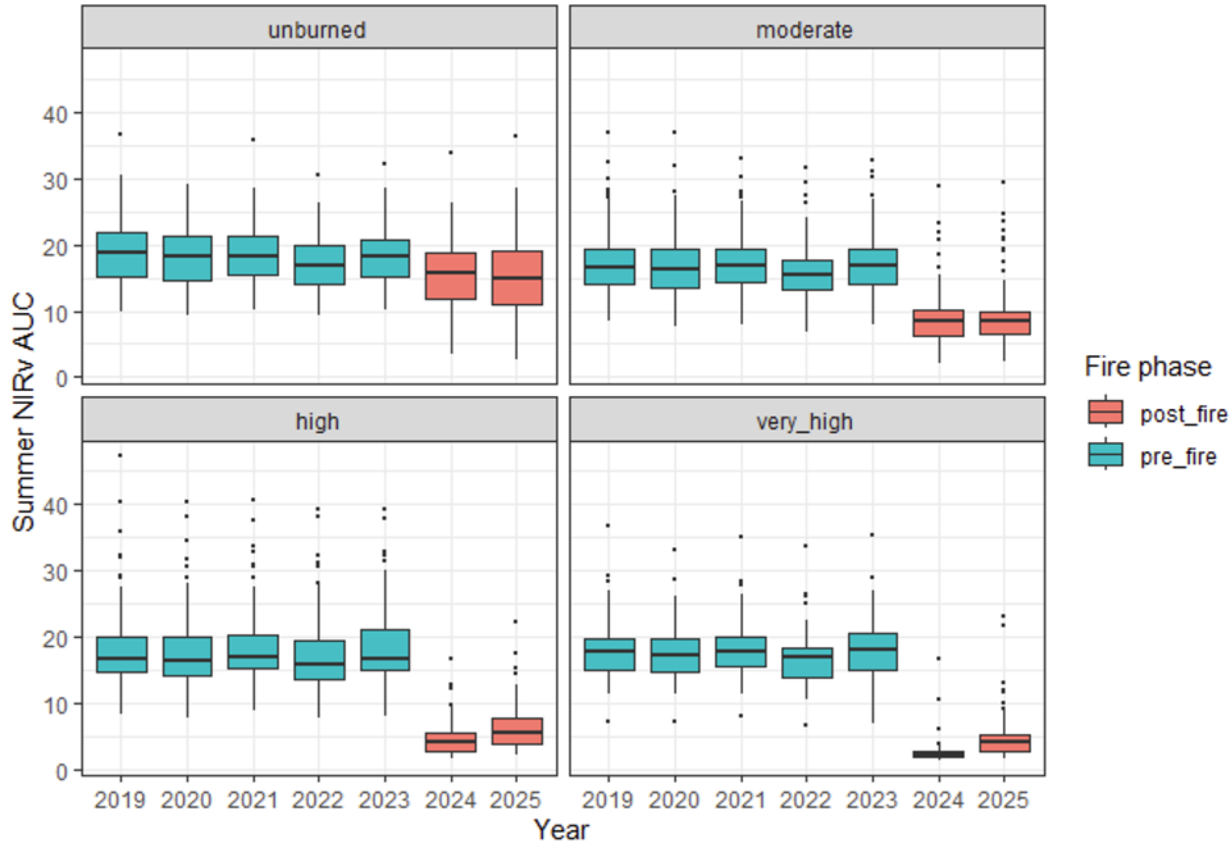

Figure S16. Pre- and post-fire summer vegetation activity across burn-severity classes. Boxplots show annual distributions of summer NIRv area under the curve (AUC) from 2019 to 2025, faceted by burn-severity class. Pre-fire years are shown in blue and post-fire years in red. Summer NIRv AUC remained broadly similar through 2023 but declined sharply after fire, with the largest reductions in high- and very-high-severity areas and smaller changes in unburned and moderate-severity areas.

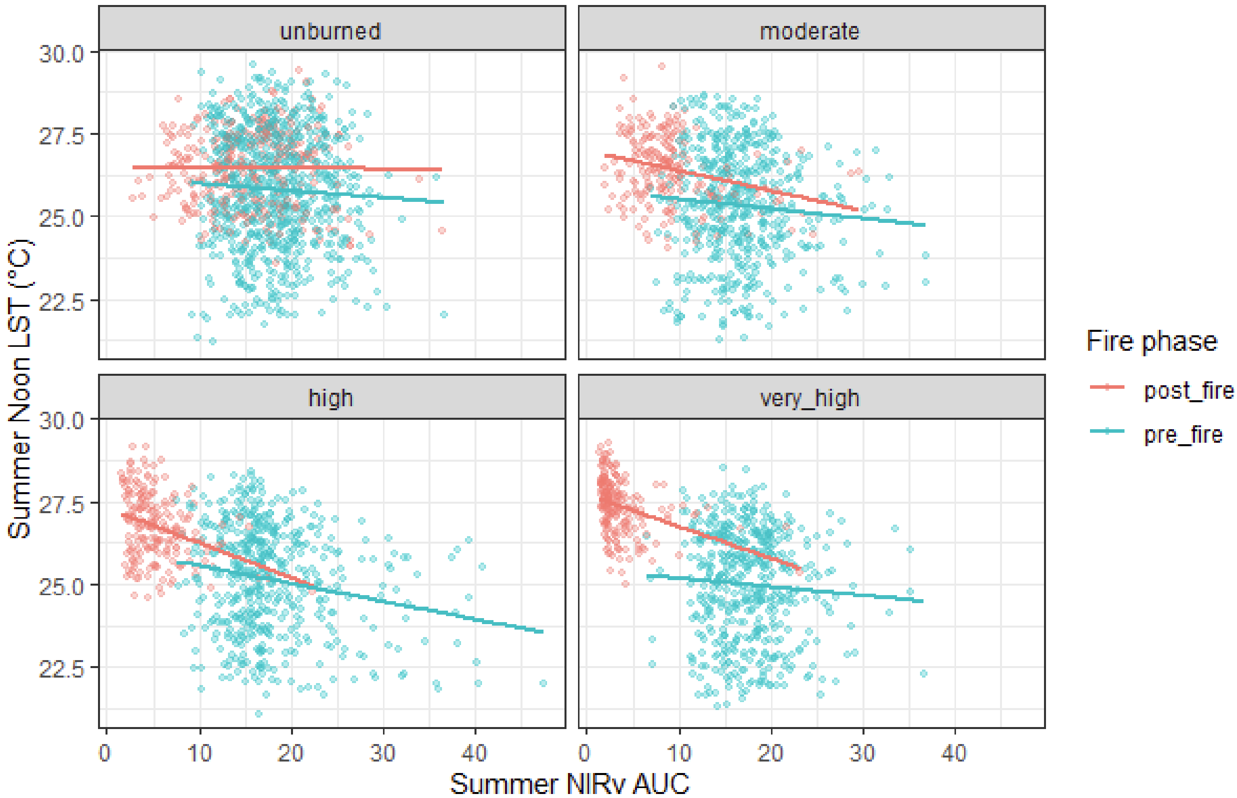

Figure S17. Relationship between summer vegetation greenness and predicted noon surface temperature before and after fire. Points show plot-level summer NIRv area under the curve (AUC) and predicted summer noon LST, faceted by burn-severity class and colored by fire phase. Fitted lines show phase-specific relationships between NIRv AUC and noon LST. Post-fire observations in high- and very-high-severity areas shifted toward lower NIRv AUC and higher noon LST, indicating strong coupling between vegetation loss and warmer surface conditions after fire.

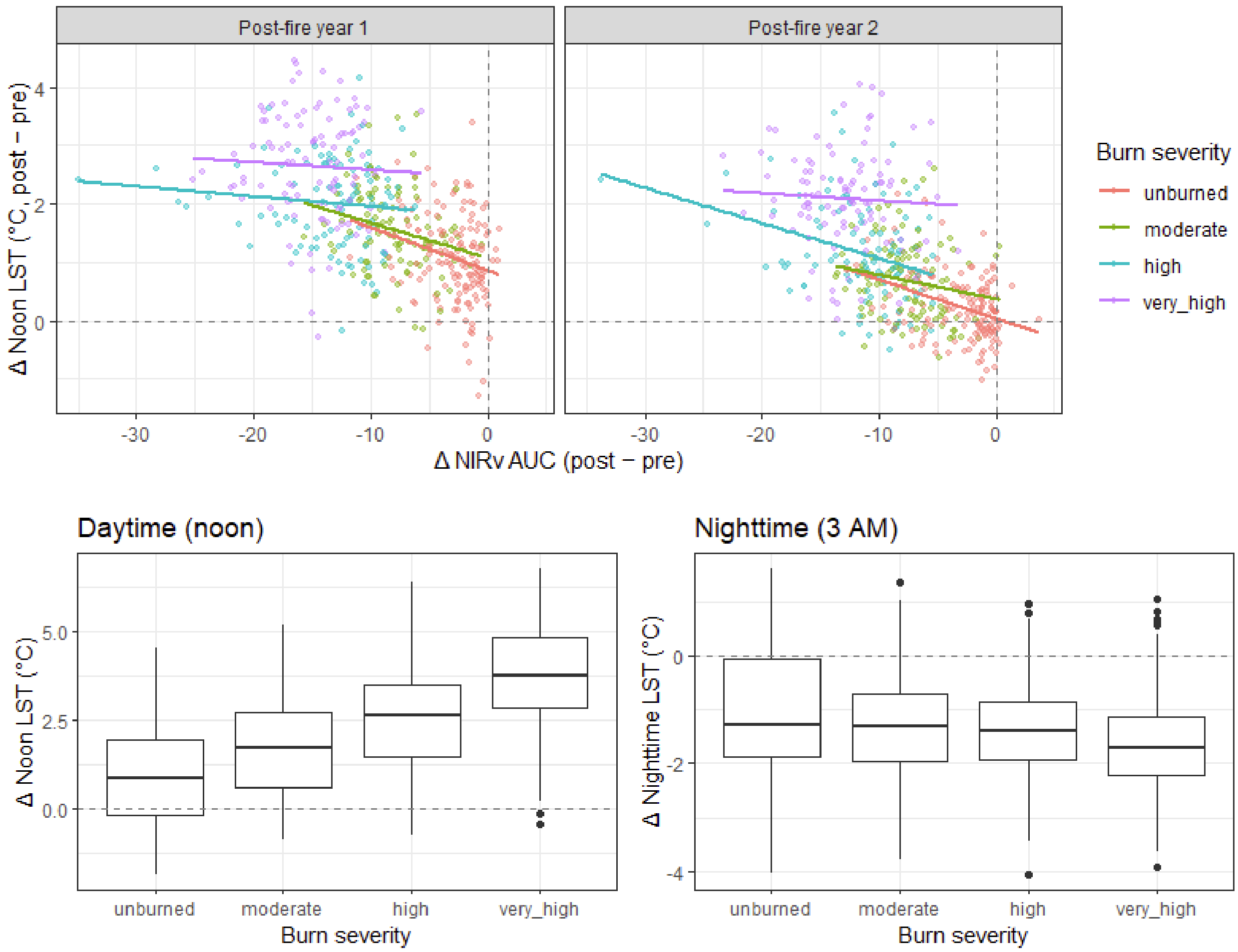

Figure S18. Post-fire changes in vegetation activity and surface temperature across burn-severity classes. (a,b) Plot-level relationships between change in summer NIRv area under the curve (Δ NIRv AUC; post-fire minus pre-fire) and change in predicted noon LST (Δ Noon LST) for post-fire year 1 (2024) and post-fire year 2 (2025), colored by burn-severity class. Dashed lines indicate no change. Larger post-fire reductions in NIRv were generally associated with greater noon surface warming. (c,d) Distributions of post-fire change in predicted daytime noon LST and nighttime 3 AM LST by burn-severity class for only observations that occur during the daytime or nighttime respectively (5:30 am to 9 pm). Daytime warming increased with burn severity, while nighttime LST generally declined across burn-severity classes.

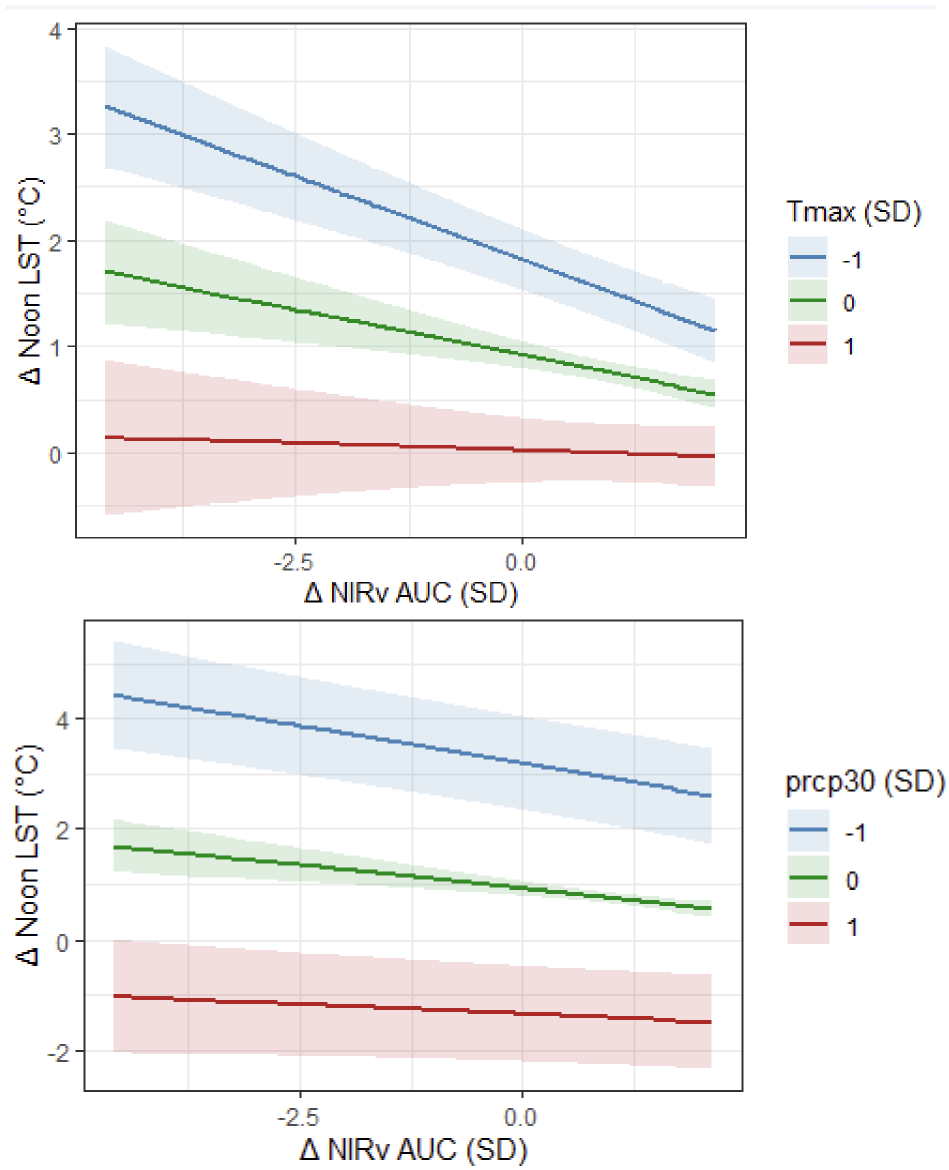

Figure S19. Climate modulation of the relationship between post-fire vegetation change and noon surface warming. (a) Model-predicted relationships between change in summer NIRv area under the curve (Δ NIRv AUC; standardized units) and change in predicted noon LST (Δ Noon LST, °C) across standardized values of maximum temperature (Tmax; top) and (b) 30-day precipitation (prcp30; bottom). Lines show predicted relationships at −1, 0, and +1 SD of each climate variable, with shaded ribbons indicating confidence intervals. The strength of the Δ NIRv AUC–Δ Noon LST relationship varied with climate conditions, indicating that post-fire vegetation loss and surface warming were coupled differently across the observed climatic gradient.